SANDIA REPORT

SAND2012-8979
Unlimited Release
Printed Month and Year

Large Core Highly Doped Fiber Amplifiers

Mark A. Dansson, Sean W. Moore, Daniel B.S. Soh, Ray P. Bambha

Prepared by
Sandia National Laboratories
Albuquerque, New Mexico 87185 and Livermore, California 94550

Sandia National Laboratories is a multi-program laboratory managed and operated by Sandia Corporation, a wholly owned subsidiary of Lockheed Martin Corporation, for the U.S. Department of Energy's National Nuclear Security Administration under contract DE-AC04-94AL85000.

Issued by Sandia National Laboratories, operated for the United States Department of Energy by Sandia Corporation.

Available to DOE and DOE contractors from
U.S. Department of Energy
Office of Scientific and Technical Information
P.O. Box 62
Oak Ridge, TN 37831

Telephone: (865) 576-8401
Facsimile: (865) 576-5728
E-Mail: reports@adonis.osti.gov
Online ordering: http://www.osti.gov/bridge

Available to the public from
U.S. Department of Commerce
National Technical Information Service
5285 Port Royal Rd.
Springfield, VA 22161

Telephone: (800) 553-6847
Facsimile: (703) 605-6900
E-Mail: orders@ntis.fedworld.gov
Online order: http://www.ntis.gov/help/ordermethods.asp?loc=7-4-0#online

SAND2012-8979
Unlimited Release
Printed Month Year

Large Core Highly Doped Fiber Amplifiers

Mark A. Dansson, Sean W. Moore, Daniel B.S. Soh, Ray P. Bambha
Org. 8128 - Remote Sensing & Energetic Materials
Sandia National Laboratories
P.O. Box 969
Livermore, California 94551-MS9056

Abstract

We have demonstrated amplification of nanosecond optical pulses to the millijoule level using ytterbium-doped phosphate glass fibers. Fibers with 35 um and 49 um diameter cores produced up to 700 uJ and 2.25 mJ pulses, respectively, with pulse durations less than 10 ns. By tapering the diameter of the fiber from single-mode to multi-mode, we were able to produce output with a nearly lowest-order-mode spatial profile in 35 um-core fibers that were inherently multimode. We report on progress in five areas of amplifier development: (1) pulse energy, (2) fundamental mode propagation in multi-mode fibers, (3) phosphate glass fiber processing, (4) highly doped gain fiber modeling, and (5) amplification of single-frequency pulses at 2 um wavelength.

ACKNOWLEDGMENTS

This work was funded by the Sandia Laboratory Directed Research and Development Program. Sandia is a multiprogram laboratory operated by Sandia Corporation, a Lockheed Martin Company, for the United States Department of Energy's National Nuclear Security Administration under Contract DE-AC04-94AL85000.

CONTENTS

FIGURES

TABLES

NOMENCLATURE

ASE	Amplified spontaneous emission
CPU	Central processing unit
dB	decibel
DFBDL	distributed-feedback diode laser
DOE	Department of Energy
EC	extended cavity
FS	fused-silica
FWHM	Full-width half-maximum
mJ	millijoule
MOPA	maser oscillator power amplifier
MFD	mode field diameter
NA	numerical aperture
Nd	neodymium
PDE	Partial differential equations
PG	Phosphate Glass
PM	Polarization maintaining
RE	Rear Earth
SBS	Stimulated Brillouin Scattering
SNL	Sandia National Laboratories
SPM	Self-phase modulation
SRS	Stimulated Raman Scattering
wt%	percent by weight
Yb	ytterbium

INTRODUCTION

1.1 Motivation

High performance pulsed lasers can perform critical tasks in remote sensing for intelligence, surveillance and reconnaissance, but suitable lasers typically have been very unwieldy. Compact lasers capable of producing diffraction-limited pulses with energies greater than a millijoule (mJ) with very narrow bandwidth are desirable but not currently available. Maser Oscillator Power Amplifier (MOPA) configurations can enable unique combinations of pulse energy and spectral properties that cannot be attained in practical single-laser systems, but suitable amplifiers are required. Optical heterodyne detection is an example of a technique that can increase the sensitivity of remote sensing system by multiple orders of magnitude, but the requirement for narrow optical bandwidth places great demands on the laser transmitter. Certain properties of fiber amplifiers make them highly desirable components in practical MOPA systems. These properties include good beam quality, ruggedness, and high power efficiency. Conventional fiber amplifiers employing fused-silica fiber are typically operated at energies less than 1 mJ, and as their outputs approach the mJ level, significant spectral distortion and broadening typically occurs. We have demonstrated significant steps in the development of fiber amplifiers that can generate energies exceeding 1 mJ with an architecture that we believe will be compatible with narrow frequency optical spectra, approaching the transform limit for 10-100 ns pulses. Amplifiers capable of generating mJ-level pulses with ultra-narrow bandwidth could potentially revolutionize remote sensing systems by enabling the wide-spread use of coherent detection. We have exploited novel phosphate glass fibers with high doping levels and large cores to demonstrate methods for fabricating suitable fiber amplifiers.

1.2 Background

Phosphate glass (PG) can accept very high doping levels of rare earth (RE) elements, and it has been used extensively in high-energy bulk lasers [1]. Recent work with PG fibers has demonstrated the benefit of these materials for single-frequency continuous wave amplifiers that produce 10 Watts average power [2] and pulsed amplifiers with over 100 kW peak power at 0.38 mJ [3]. Because the maximum range for detection in a remote sensing system is a function of the transmitted energy, higher pulse energies are generally desired to increase stand-off distances.

The overwhelming majority of past fiber amplifier work has used fused-silica (FS) fiber, which was facilitated by well-developed fiber fabrication and processing technology. However, compact devices with high energies have been elusive because of limitations to the maximum doping in FS fibers of ~1%. Step-index or graded-index fiber amplifiers require lengths ≥1 meter to produce the highest energies, which are limited by the onset of Stimulated Brillouin Scattering (SBS) and Stimulated Raman Scattering (SRS). Energies in FS fiber amplifiers with low M^2 have typically been less than 1 mJ, and on a rare occasion have exceeded 1 mJ [4, 5]. Although higher energies (up to 4.3 mJ) and good beam quality have been achieved in photonic crystal fibers with large mode areas, these devices also require rigid rods of costly structured glass with lengths approaching 1 meter [6], which severely limits their practical uses. In contrast PG can accept substantially higher doping than FS, which can greatly shorten the required length of a PG

fiber with comparable gain. A short (~10 cm) PG fiber amplifier will be essentially free of SBS and line-broadening effects [3].

Another method for reducing the effects of nonlinearities in fiber amplifiers is the use of fibers with large cores that reduce the peak intensity. Because diffraction-limited output is typically desired, suppression of higher-order modes is generally required in order to employ fibers with large cores that inherently support multiple modes. Fused-silica fiber amplifiers are typically long enough that coiling of the fiber is possible and bend-loss induced mode filtering can be used effectively [5]. For short (~10 cm) PG fibers, this technique is not available, and therefore inherently single-mode fibers with low numerical apertures have been employed in the past [3]. Alternatively, the lowest-order mode can be excited selectively under proper launching conditions, and the lowest order mode can propagate for substantial lengths (>> 10 cm) if the fiber remains straight and uniform [7]. The fibers used for the work presented here were generally multimode, and selective amplification of the lowest order mode in short straight fibers was demonstrated.

1. EXPERIMENTAL

2.1 Energy Scaling

2.1.1 Gain fibers

We performed amplification measurements with phosphate glass (PG) fibers with two different doping levels of Yb, 20 wt% (percent by weight) and 5 wt%. These fibers were fabricated from rod-in-tube preforms, which are commonly used for fibers fabricated from multicomponent glass (Fig. 2.1). The core and cladding glasses were fabricated separately and fused together during the fiber drawing process. The manufacturer (Kigre, Inc.) engineered the glass compositions to achieve our specified properties of doping and numerical aperture (NA) while simultaneously matching the thermal expansion of the core and cladding glasses. The process of determining suitable glass compositions requires iterations, and as a result, a trade-off exists between achieving a specific numerical aperture and fabricating the fiber under cost and time constraints. The actual numerical apertures of all of our fibers were higher than our requested target of 0.025. The 20 wt% doped fiber NA was approximately 0.13, while the NA of the 5 wt% doped fiber was approximately 0.05. Each of the preforms was drawn to two different fiber diameters to produce our desired core/cladding diameters. The outer diameters for the two fiber sizes (core/cladding) were 35 / 125 µm and 49 / 175 µm. The fibers were double-clad with an outer cladding of low-index optical polymer that the guided pump light in our cladding-pumped amplifiers. As discussed below, the fibers with 20 wt% doping exhibited low gain, and most of the work was performed on the 5 wt% doped fibers.

All of the PG fibers fabricated for this effort were inherently multimode. The number of modes, N_{modes}, supported by a fiber with radius a can be estimated using the equation [8],

$$N_{modes} \approx \frac{4}{\pi^2} V^2 \quad \text{where} \quad V = \frac{2\pi a}{\lambda} NA.$$

For the 5 wt% doped fibers the number of modes supported by the fibers was approximately 11 for the 35 µm core fiber and 23 for the 49 µm core fiber. In order to achieve good beam quality using these fibers we investigated selective excitation of the lowest order mode using tapered fibers and free-space launching of carefully formatted input beams. Tapering proved to be highly effective, but suitable tapers for our 49 µm core fibers could not be fabricated due to the high NA and equipment limitations on the lengths of tapers. Ultimately, we were able to propagate low-order modes in the 35 µm core fibers only. Fabrication of PG fibers with lower NA should be possible with further engineering, and therefore low-order mode propagation in larger cores may be feasible.

We investigated the effect of input pulse duration on output energy using a series of master oscillator (seed) sources. Pulse durations ranged from 0.5 ns up to approximately 10 ns. The general trend we observed was that the output energy was limited by optical damage near the output end of the gain fiber, and higher energy was obtained using longer pulses.

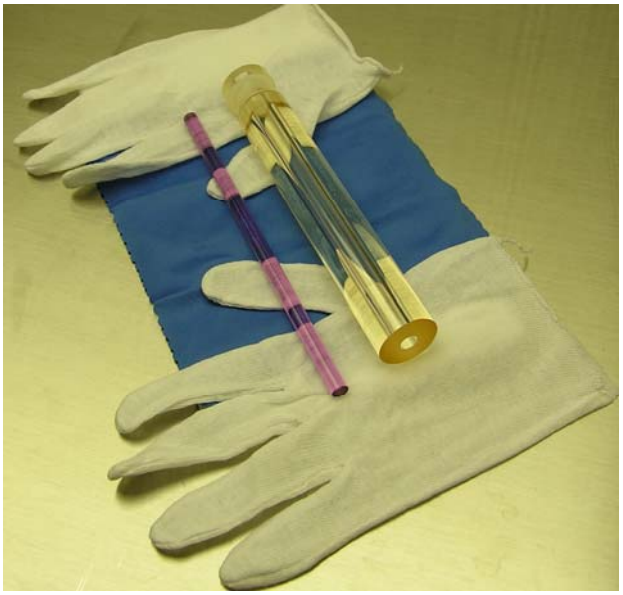

Figure 1.1 Example of a rod-in-tube phosphate glass preform with Nd-doped core rod.

2.1.2 Results

The first amplifier input source we employed was a passively Q-switched Yb:YAG laser fabricated at Sandia with a pulse duration of approximately 0.5 ns pulse and energy of 30 µJ. We used a FS fiber amplifier to increase the seed energy to 210 µJ for some of the experiments. We cladding-pumped the PG fibers with a fiber-coupled diode bar operating at 975 nm, and we launched up to 11 W in these experiments. The maximum energy extracted from the 20 wt% Yb-doped 35 µm core fiber prior to damage was 310 µJ with 210 µJ input, which indicated very low gain the 20 wt% fibers. By comparison the maximum energy extracted from the 5 wt% Yb fiber was 350 µJ with 35 µm core using 30 µJ input, indicating that the 5 wt% doping was higher performance than 20 wt%. The remainder of our work was performed using the 5 wt% doped fibers. The 350 µJ output from the 5 wt% Yb fiber also could be contained predominately in lowest order spatial mode, if we employed a tapered FS fiber to launch the input.

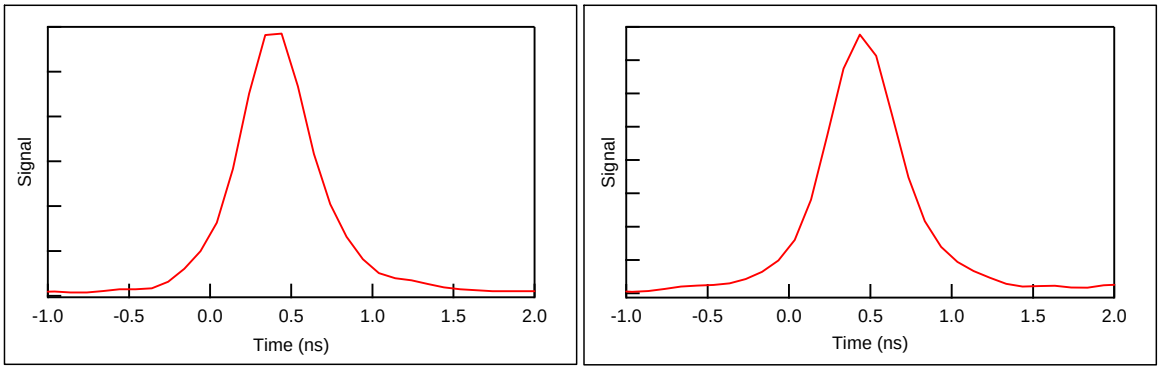

Figure 1.2 Temporal profiles measured using the 0.5 ns micro-laser oscillator. A) 30 µJ micro-laser pulse prior to amplification B) 180 µJ amplified micro-laser pulse.

Using a seed source of approximately 1 ns duration at 1030 nm wavelength, we attained energies of 205 µJ and 400 µJ for the the 35 µm and 49 µm core diameter 5% Yb PG fibers, respectively, prior to damage. The input to the 35 µm core fiber was launched using a butt-coupled tapered FS fiber, and the output was predominately in the lowest order mode. For the 49 µm fiber the input was launched through free space, which lead to multimode propagation. We observed substantial variation in the damage threshold, and we determined pulses durations of ~10 ns or greater would be necessary to attain multi-mJ output.

In an attempt to improve energy extraction from the PG amplifiers, we built a Yb-doped FS fiber laser capable of generating pulses with durations much greater than 1 ns. The output temporal profile of the fiber laser generally had two closely spaced lobes with individual durations of 5-10 ns. Figure 2.3 is an example of the temporal behavior of the fiber laser, showing short-duration peaks superimposed on the two-lobe structure. Using this fiber laser as the master oscillator, we attained the highest output powers from our PG fiber amplifiers. The maximum output was 2.25 mJ, which was achieved using a 31 cm gain segment with 49 µm core diameter and 5% Yb doping, and input energy was 25 µJ. With this same seed laser, the highest output pulse energies from 35 µm core PG fiber (5 wt% Yb doped) was approximately 660 µJ. Optical damage generally limited the attainable output energy using the fiber laser input.

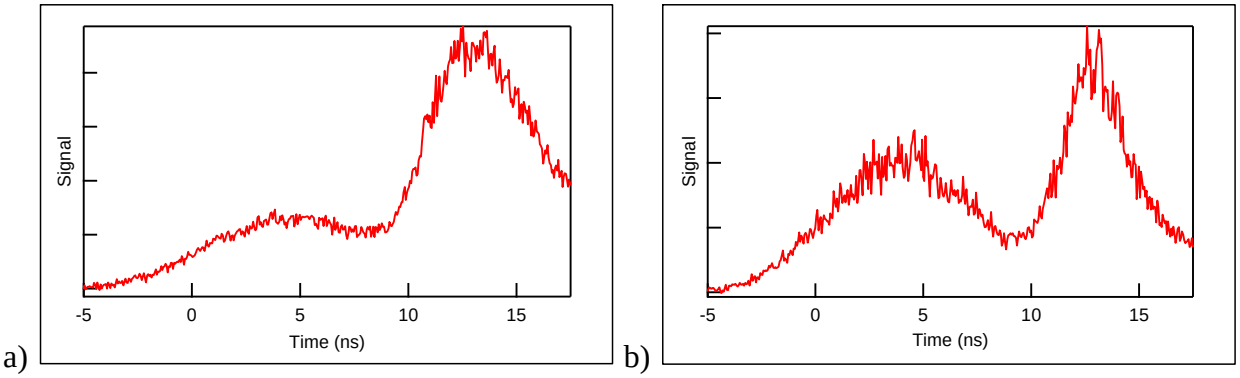

Figure 1.3 Temporal profiles measured using the fused-silica fiber-laser oscillator, a) 25 µJ input pulse b) output pulse amplified to 2 mJ.

We built a passively Q-switched Yb:YAG laser with an extended cavity (EC-microlaser) to produce a smooth temporal profile of approximately 10 ns duration (fig. 2.4). The 35 µm core (5 wt% Yb) PG fiber produced 700 µJ pulses with fundamental mode output (Fig. 2.5), while the 49 µm core fiber achieved over 1.4 mJ pulses before damage (Fig. 2.6). The fundamental mode was selectively transmitted through the tapered 35 µm core (5 wt% Yb) PG fiber using the EC-microlaser as the input. With a 19 cm multi-mode gain section, the fundamental mode amplifier obtained 430 µJ before gain saturated with increasing pump power, and damage was not observed. Further testing was not conducted to increase the length of the fiber and potentially increase the output energy with single-mode operation.

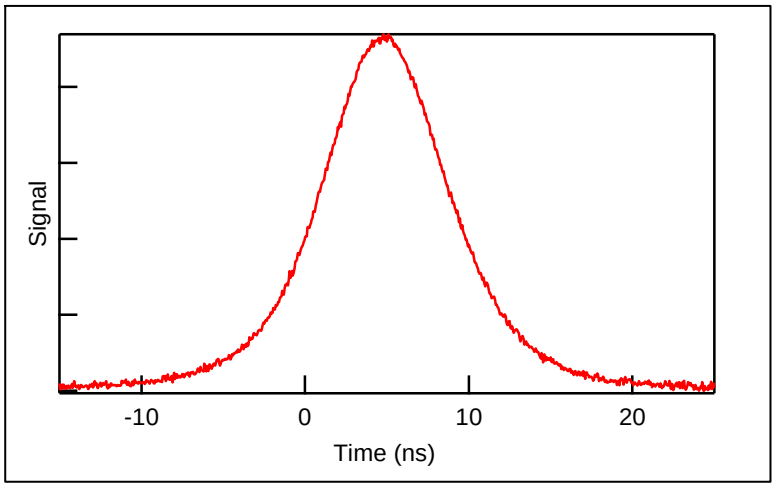

Figure 1.4 Temporal profiles of the 9 ns Extended cavity micro-laser output.

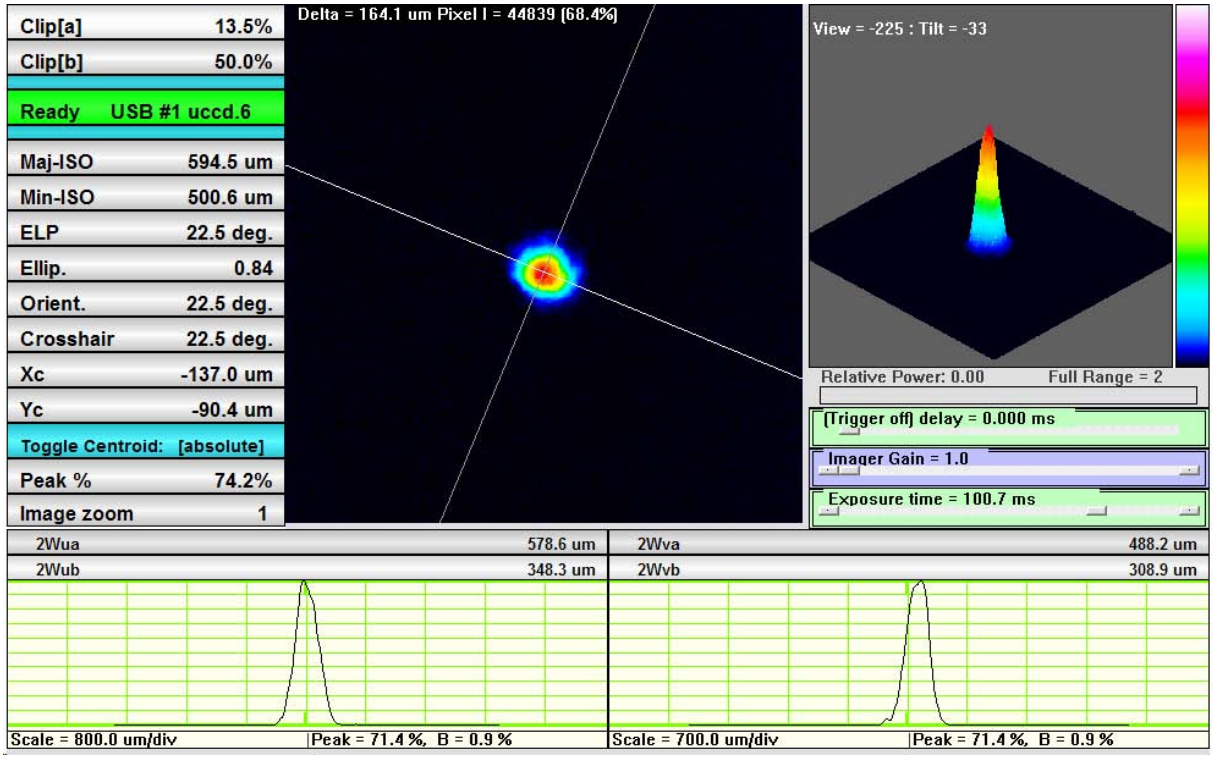

Figure 1.5 Example of a beam profile measurement following low-order mode amplification in a multimode PG fiber. The output mode propagated through a 10 cm length of 35/125 µm 5% Yb PG fiber by free-space launching a pre-amplified beam. It is a near-fundamental mode, indicating that free-space launching into the multi-mode fiber can obtain low-order modes if well matched. This energy in this mode was measured to be 700 µJ.

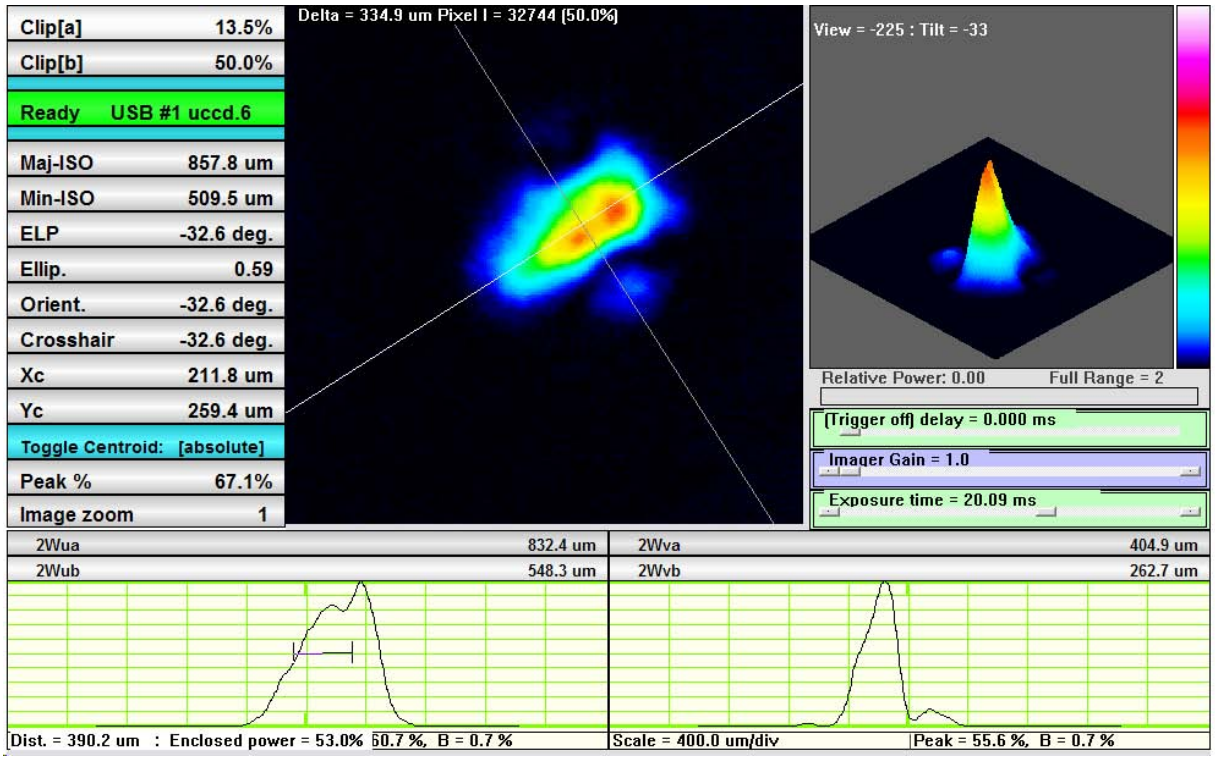

Figure 1.6 Example of a beam profile measurement from a multimode beam amplified in a multimode PG fiber. The above pictured mode is a view of the mode in the core of the 49/175 µm 5% Yb PG fiber achieved via free-space launching. This was the approximate mode during the run achieving 1.4 mJ with the extended cavity laser.

The lower output level before damage for the EC-microlaser seeded PG amplifier compared to the fiber laser seeded case is consistent with the shorter overall pulse duration of the EC-microlaser. Based on our various measurements we estimate a damage threshold 250W/µm^2 at the peak intensity of the pulse for the 49 µm core fibers, which is generally consistent with the estimate provided by Kigre of 25 J/cm^2 (1 ns pulse). We found the maximum attainable energies were highly variable, and they appeared to increase more rapidly than the mode area when we compare results for PG fibers with 35 µm cores to those with 49 µm cores.

2.2 Fiber Processing

We cleaved our PG fibers using a Vytran LDC-400 cleaver. While cleaving tension is well characterized for FS fiber, PG fiber is much softer and needs to be cleaved under much lower tension. We found that the appropriate tension was between 60% and 75% of the tension required to cleave a FS fiber of the same diameter. Because of the brittle nature of PG, extra care was required to ensure that all cleaver components were free of debris during clamping and cleaving.

Splicing was performed with the Vytran GPX-3000 glass processing system. Successful splicing was of the 35 μm core PG fiber produced only minor distortion of a fundamental mode. Testing was performed on a straight piece of PG fiber with both the input and output selectively transmitting the fundamental mode. After cleaving the PG fiber in the middle, we butt-coupled the two halves of the PG fiber, and selective transmission of the fundamental mode transmission was verified (Fig. 2.7), demonstrating a high quality cleave. The two halves were then fusion spliced, and the mode transmission was again observed to be fundamental.

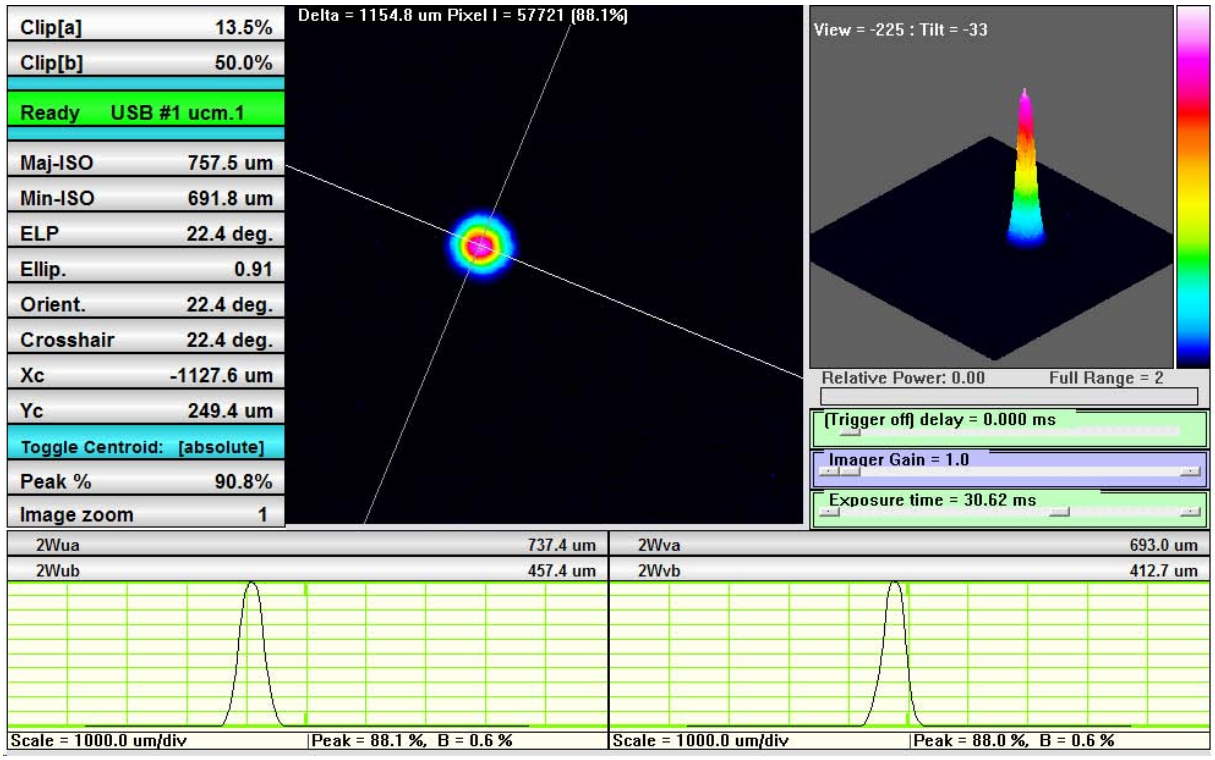

Figure 1.7 Example of a beam profile measurement of a single piece of 35 μm core PG fiber, cleaved and respliced.

Low-order mode propagation in multimode fiber was achieved using a tapered input. The taper allowed the light from the oscillator to be launched through a single mode section of fiber, and the lowest order mode propagating through the fiber expanded as the fiber diameter increased in

a tapering section of the fiber. We employed two approaches to tapered inputs. One approach was to fabricate the taper in FS fiber with an output mode field diameter (MFD) nearly matched to the PG MFD (Fig. 2.8). The second approach was to taper the actual PG gain fiber (Fig. 2.9).

We performed numerous iterations of the PG fiber tapering process to determine the best fiber preparation procedure and settings for the Vytran fiber processing station. We found that the preparation of the fiber prior to tapering was extremely important to avoid damaging the fibers or having fiber segments with residual bends. The preparation process involved stripping the coating and chemically cleaning the residual coating with a 2% Hellmanex II solution in deionized water. Straightening the fiber prior to tapering by heated annealing appeared to improve the tapering process. Selection of the correct power level and tapering rate were critical to achieving successful tapering.

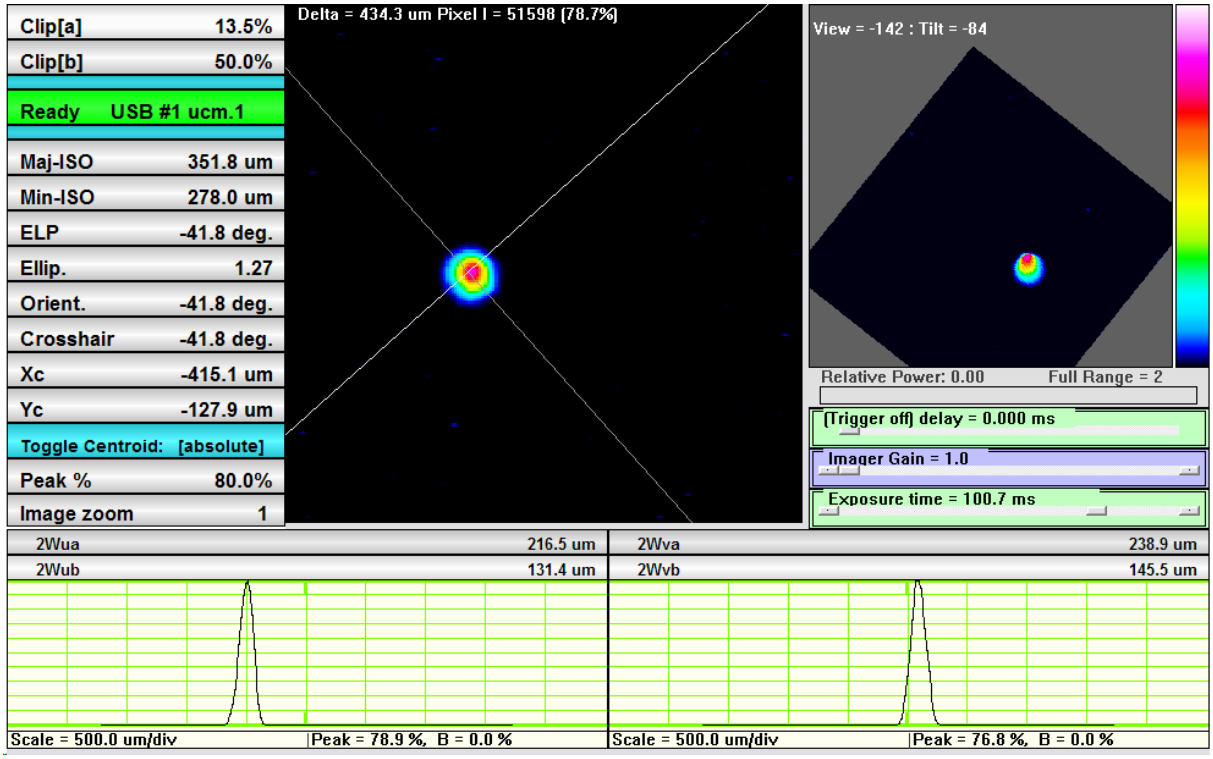

Figure 1.8 Example of a beam profile measurement following low-order mode propagating through a multimode PG fiber using a tapered fused-silica fiber input. Fused-silica fiber (30/250 µm) was tapered down to 60 µm OD producing a 5 cm long section that functioned as a filter for non-fundamental modes. The multimode section of the fused-silica fiber was butt-coupled to the 35/125 µm 5% Yb PG fiber 20 cm long.

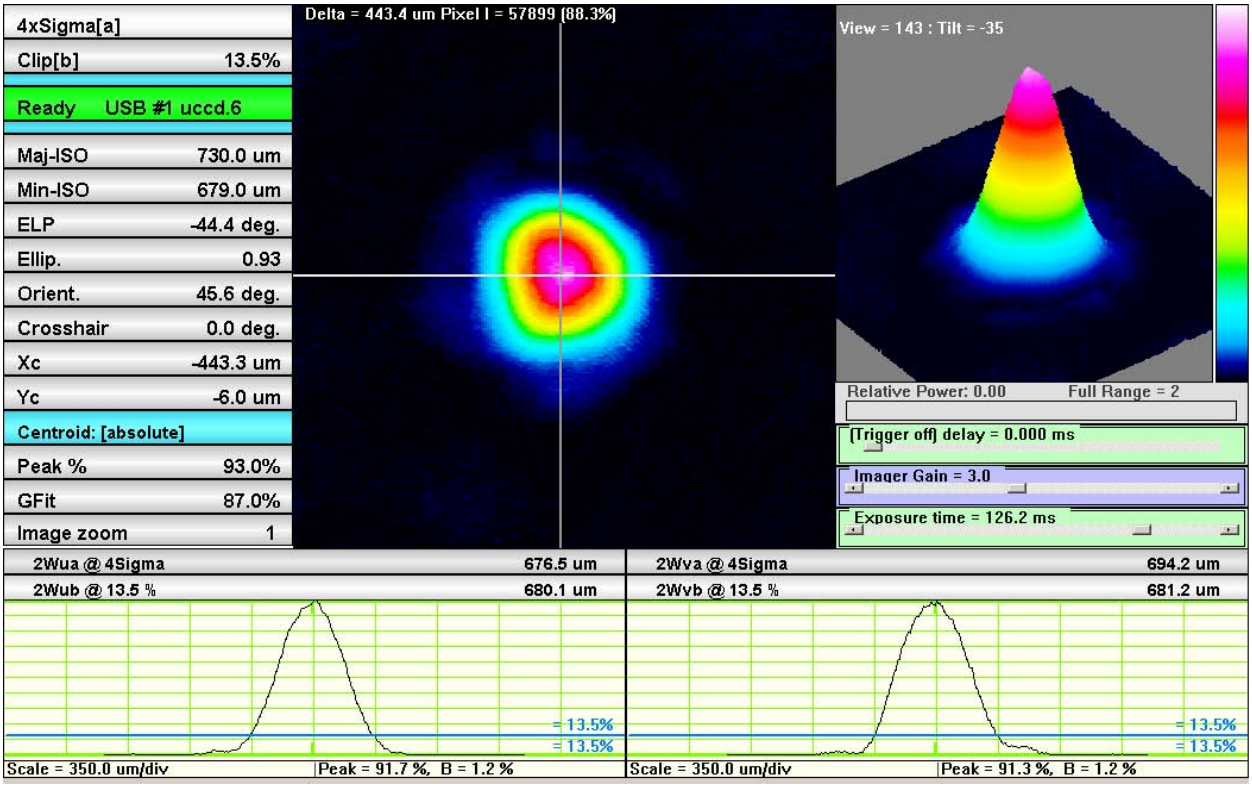

Figure 1.9 Example of a beam profile measurement following low-order mode propagating in a multimode PG fiber through the use of a tapered PG fiber input. A free-space input beam was launched into a 5 cm long 9.8/35 µm PG single-mode section of a tapered 35/125 µm 5% Yb fiber. The single-mode section was followed by a 15 mm up taper to a 10 cm long multimode 35/125 µm section.

2.3 Fiber amplifier development for the 2 µm region

We conducted a series of experiments to study amplification of very narrow-band, wavelength-tunable pulses at 2 µm using an architecture that included a highly doped silicate fiber amplifier. Figure 2.10 is a block diagram of the MOPA architecture that we used. The master oscillator was a distributed-feedback diode laser (DFBDL) operating at 2.05 µm. The DFBDL output power was approximately 1 mW, and, according to the vendor (Nanoplus, GmBH), the linewidth was approximately 1 MHz. The output of the diode laser was amplified in a thulium-doped FS fiber (Nufern PM-TDF-10P/120-HE). The Tm-doped FS fiber was cladding-pumped by a fiber-coupled 793 nm diode laser and produced approximately 30 dB of gain. A free-space coupled Pockels-cell modulator (Fastpulse Technologies) placed after the first amplifier formed pulses with variable duration from 200 to 500 ns. The final stage was an amplifier using Tm-Ho codoped silicate fiber (Advalue Photonics.). The silicate fiber was approximately 1 m in length and doped at approximately 7 wt%. Cladding pumping at 793 nm of the Tm dopant in the Tm-Ho co-doped silicate fiber resulted in excitation of the Ho ions, which provided the gain at 2 um [9].

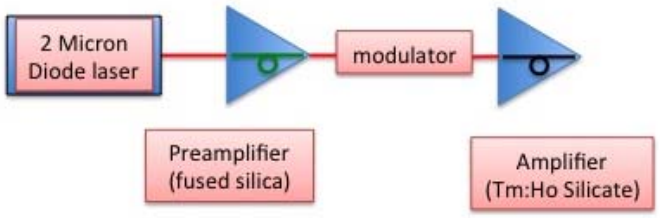

Figure 1.10 Block diagram of the single-frequency 2 µm MOPA system.

We made gain measurements for both amplifier stages. Figure 2.11 is a plot of the gain of the FS amplifier, which produced a maximum gain of approximately 30 dB before the gain began to saturate. Figure 2.12 is a plot of the gain for 200 and 500 ns pulses for the Tm:Ho silicate amplifier. The gain of the silicate amplifier was approximately 20 dB leading to approximately 3 µJ pulsed (200 ns).

This work demonstrated the first stages of a versatile seed source that will be needed to exploit the benefits of large core highly doped fiber amplifiers. Our design for future development calls for a second silicate amplifier identical to the existing one to be placed after at the output of the current system to generate approximately 0.3 mJ pulses. This would provide suitable input for a multi-mJ large-core amplifier, and the overall system is expected to be capable of single-frequency operation.

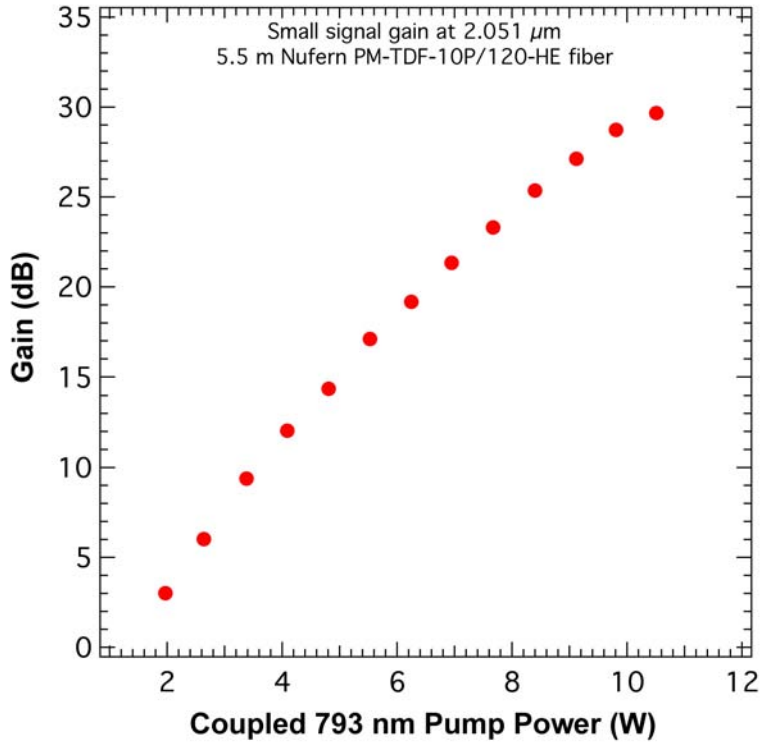

Figure 1.11 Continuous-wave power gain for the Tm-doped fused-silica preamplifier.

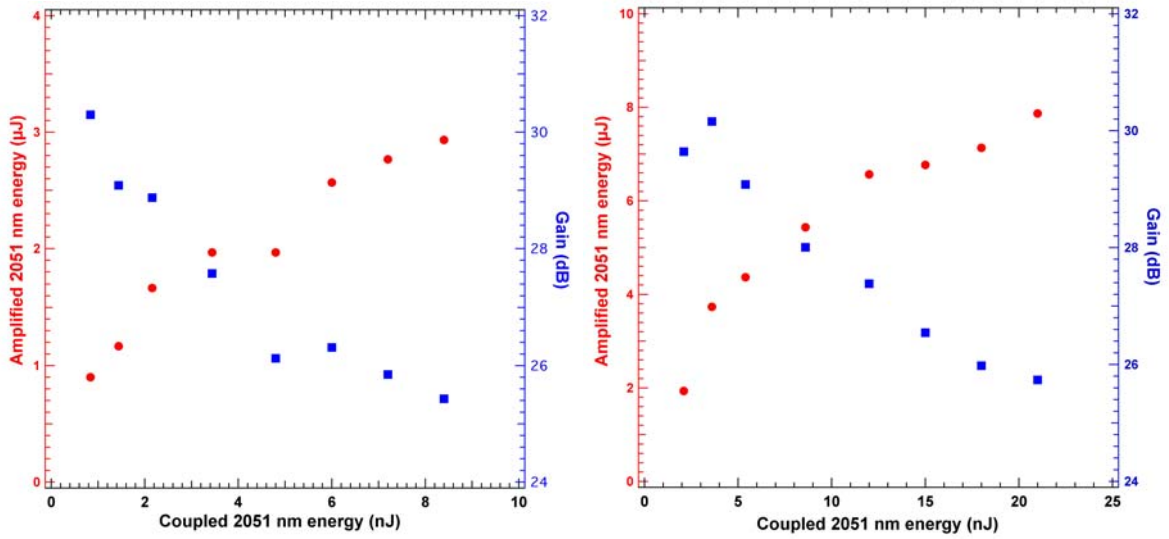

Figure 1.12 Gain and pulse energy for the Advalue Tm-Ho silicate fiber amplifier using a 5.5 m Nufern PM-TDF-10P/120-HE fiber pre-amplifier.

2. MODELING PHOSPHATE GLASS AMPLIFIER

3.1 Modeling

3.1.1 Background

During the course of experimental efforts, it was noted that the behavior of the PG optical amplifier could not be understood well with the existing modeling tools. Several different numerical simulators were tested. These included Arlee's ZT model based numerical simulator [10] and other commercial fiber amplifier software. A major discrepancy between the experimental data and the results of numerical simulators was the optical efficiency.
A numerical simulator was desired which we understand clearly and can modify easily. First, a good model, based on well-defined assumptions, needed to be developed. It was critical to clearly state the assumptions made, in order to debug the modeling through comparison with the experiments.

3.1.2 Basic information of the optical amplifier

The PG optical amplifier was originally developed for pulse amplification. It was intended that the optical amplifier would operate in single transverse mode to ensure a good output beam quality, although the core waveguide supported multiple modes. The amplifier fiber considered was a Yb^{3+}-doped PG cladding pumped device. The advantages of the suggested device can be summarized as follows:

- The PG can hold orders of magnitude higher active dopant concentrations without serious performance degradation through quenching. Hence, the device length can be *extremely short*, compared to conventional low doped fiber amplifiers.
- Since the device length is reduced, one can essentially *operate in a single transverse mode*, when the seed optical source is coupled almost exclusively into the fundamental transverse mode of the PG waveguide. Mode mixing will not be detrimental due to the short amplifier length.
- The optical nonlinearity is mitigated in two orthogonal ways: core area expansion and amplifier length reduction. Thanks to the reduced nonlinearity, one can *achieve larger optical pulse energy* with better spectral/temporal quality.

Table 1 summarizes the parameters of the PG amplifiers modeled. It is noted that the cores of the two fibers support multiple guided modes since the calculated normalized propagation constant V is larger than 2.405 in both cases. Specifically the V numbers are 7.7 for Fiber 1 and 15.4 for Fiber 2 at 1005 nm.

	Fiber 1	Fiber 2
Core diameter [μm]	35	70
Core NA	0.07	0.07
Cladding diameter [μm]	125	175
Doping concentration [Yb_2O_3 wt %]	5, 20	5, 20

Table 2.1Summary of parameters for the Yb3+ doped phosphate glasses

For modeling and simulation, we needed to convert the doping concentration from Yb_2O_3 wt % into the number of Yb^{3+} ions per unit volume. Yb^{3+} ions are part of Yb_2O_3 molecular structure, which has molecular mass of 373.98 g/mol. The PG has a dominant molecular structure of P_2O_3, which has 310.14 g/mol. If we assume the glass density as 2.45 g/cm^3, we can calculate the number of ions as a function of doping concentration. Suppose we have 1 m^3 volume of glass, which is doped with 1 wt % of Yb_2O_3. Then, we have 24500 g of Yb_2O_3 molecules in the 1 m^3 volume. Thus, we have 65.5 mol of Yb_2O_3 molecules, which translates to 3.95 $\times 10^{25}$ molecules, with the Avogadro constant 6.022×10^{23} ions/mol. Then, we have 7.89 $\times 10^{25}$ Yb^{3+} ions/m^3 for each 1 wt % Nd_2O_3 doped glass. The following summarizes the conversion from doping concentration to density of active ions.

$$1\ (Yb_2O_3)\ \text{wt \%} = 7.89 \times 10^{25}\ (Yb^{3+})\ \text{ions/m}^3. \tag{3.1}$$

3.1.3 Guided modes of fibers

We can obtain the guided modes of these fibers, using the method in reference [11]. The method adopts Bessel functions as the eigenfunctions for the Helmholtz equation. The following is a very brief introduction to the method to obtain the eigenfunctions and the associated eigenvalues of the Helmholtz equation. The electrical field of the guided light can be expressed as

$$E(r,\phi) = E(r)\cos(\nu\phi), \tag{3.2}$$

where (r,ϕ) represents the cylindrical coordinate (radius and angle). If we separate the variables as above, one can extract the radial differential equation:

$$\frac{d^2E(r)}{dr^2} + \frac{1}{r}\frac{dE(r)}{dr} + \left[n^2(r)\frac{\omega^2}{c^2} - \beta^2 - \frac{\nu^2}{r^2}\right]E(r) = 0, \tag{3.3}$$

where $n(r)$ is the refractive index profile as a function of radius coordinate, ω is the optical angular frequency, c the speed of light in vacuum, and β the propagation constant (eigenvalue to obtain). In equation (3.3), we allowed the variation of the refractive index along the radial position. If we introduce a functional space with an orthogonal basis constituted from Bessel functions, it is straight forward to demonstrate that the functional space is complete, becoming a Hilbert space. Then, any solution $E(r)$ can be represented through a superposition of the bases as

$$E(r) = \sum_{\mu=1}^{\infty} c_\mu J_\mu(\kappa_\mu r), \tag{3.4}$$

where c_μ are the weights, J_μ are the Bessel function of the first kind in order μ, κ_μ are related to the roots of the Bessel functions w_μ by $\kappa_\mu = w_\mu / R$ where R is the core radius. By putting equation (3.4) into (3.3), one can obtain all the eigenfunctions (i.e. sequences of c_μ's, defining eigenfunction $E(r)$) and the associated eigenvalues (β's). This is accomplished by equating recursive matrix equations.

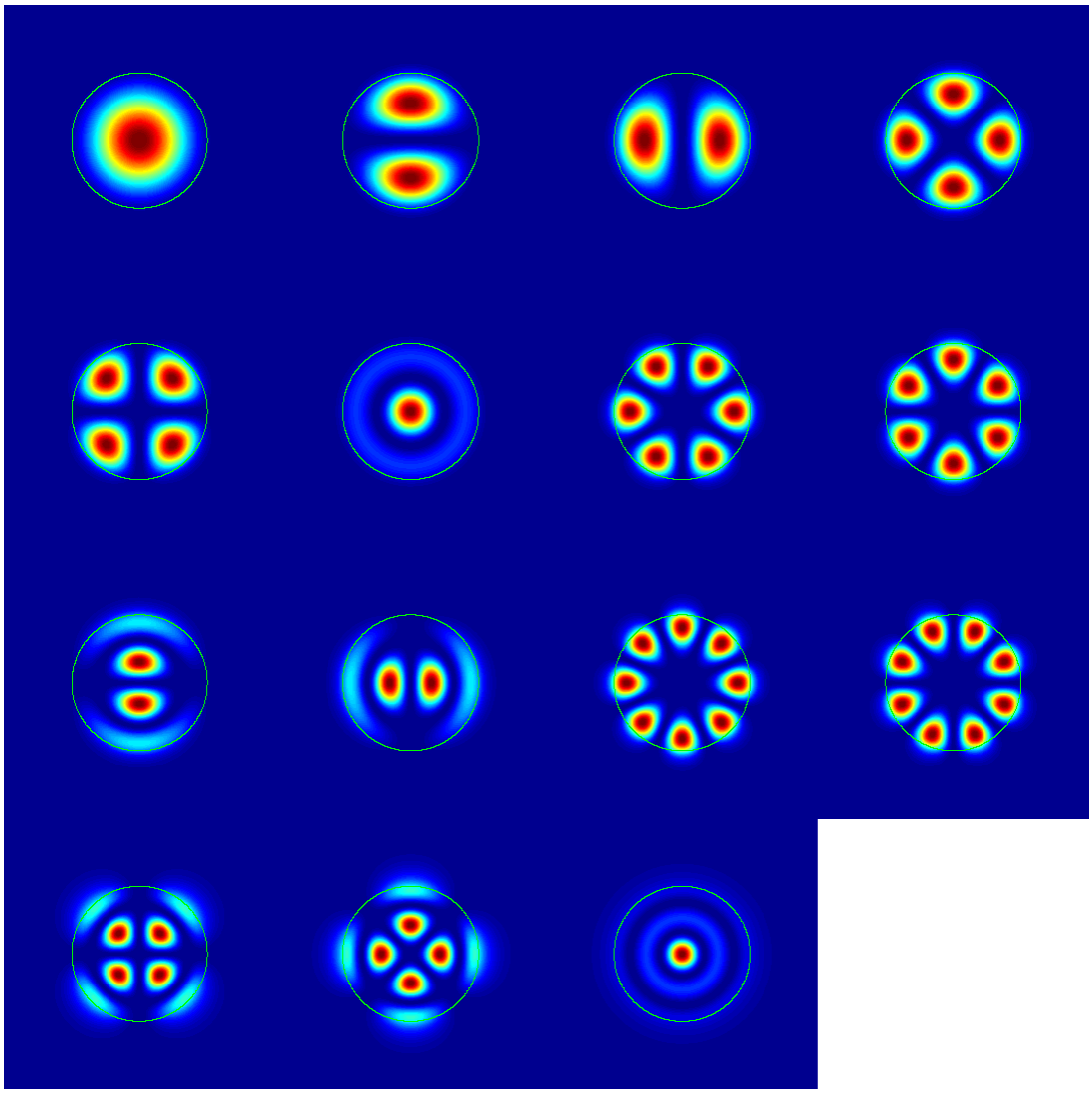

Figure 2.1 Intensity profiles of orthogonal guided modes of Fiber 1 at 1005 nm.

Based on this method, we obtained the guided modes with the fiber dimension in table 3.1. We assumed the wavelength at 1005 nm and the result is shown in figure 3.1. There are 15 orthogonal guided modes. Please note that there are 'sine' modes and 'cosine' modes, which are

rotated by 90 degrees to each other and are orthogonal in ψ direction. The nomenclature of the modal names is $LP_{\mu\nu}$ modes, with μ represents the Bessel function order and ν represents the angular order. The names of the modes and the corresponding effective numerical aperture of the modes, which are defined by $NA_{eff} \equiv \sqrt{n_{eff}^2 - n_{cl}^2}$ where $n_{eff} \equiv \beta c/\omega$, are shown in table 3.2. Since the fiber is short, we did not calculate the bending losses. However, if it is necessary, one can calculate the bending losses for each mode based on the method in references [12-14].

LP_{01} (0.067)	LP^{s}_{11} (0.063)	LP^{c}_{11} (0.063)	LP^{c}_{12} (0.056)
LP^{s}_{12} (0.056)	LP_{02} (0.054)	LP^{c}_{13} (0.047)	LP^{s}_{13} (0.047)
LP^{s}_{21} (0.042)	LP^{c}_{21} (0.042)	LP^{c}_{14} (0.034)	LP^{s}_{14} (0.034)
LP^{s}_{22} (0.022)	LP^{c}_{22} (0.022)	LP_{03} (0.018)	

Table 2.2 Names of the modes shown in figure 3.1 and the associated effective NA. $LP^{c,s}$ represents the cosine and the sine modes, respectively.

We also obtained the guided modes for Fiber 2. The number of guided modes is 61 at 1005 nm. The intensity profiles of the guided modes for Fiber 2 are shown in the figure 3.2.

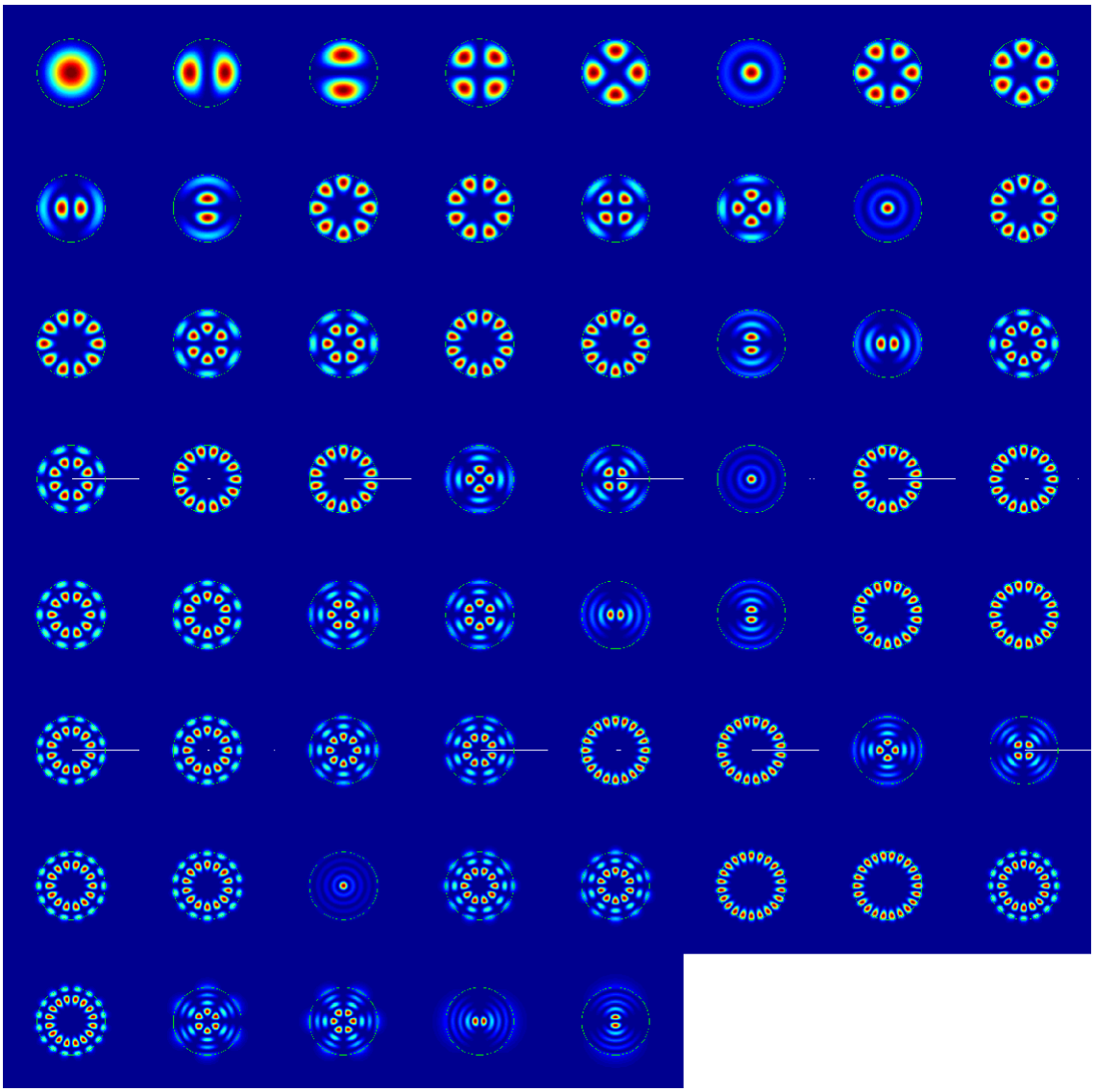

Figure 2.2 Intensity profiles of orthogonal guided modes of Fiber 2 at 1030 nm.

3.1.4 Assumptions of modeling

In this section, we clarify the assumptions made for modeling the PG amplifier. Depending on the regime of operation, we can simplify the model greatly and reduce the simulation burden to obtain the result quickly with reasonable accuracy. Obtaining an accurate result in a reasonable simulation time is especially important when we use the numerical simulator for optimizing the design parameters, where we have to study the entire parameter space of concern. Sometimes the parameter space may have greater than 3 dimensions. In this case, the simulation time for a single set of parameters is critical.
We will model the following properties of the fiber amplifier:

- Multiple transverse guided modes and their effects on the spatially resolved (both radius

and angle) inverted population distribution in a doped core.

- Spectrally resolved signal/ASE power with measured stimulated emission and absorption cross-sections and the lifetime of the excited state
- Spontaneous emission and its capture by each guided modes.
- Partial differential equation (time and position) for the propagating pulse inside the amplifier.

The following physics are ignored since the amplifier will be operating in a regime where the following effects will be negligible.

- Radiation loss of the guided mode: We will not consider the bending loss for the guided modes since the amplifier fiber is assumed to be sufficiently short and it will be straight.
- Mode mixing: Since the fiber is very short ($\ll$ 1 m) and the number of guided modes are rather small (i.e., the difference between the propagation constants of guided modes is rather large), the mode mixing is ignored.
- Polarization dispersion: Since the fiber is very short ($\ll$ 1 m), the polarization dispersion effect will be ignored. In addition, any dispersion effect will be ignored.
- Stimulated Rayleigh scattering: The fiber is short enough to ignore this effect.
- Finite response time of light-matter interaction: Since the signal pulse is longer than nanosecond, we will ignore the transition time of atomic energy state. Therefore, the conventional rate equation is used.

The following items are not considered at the moment, but will be considered in the later development phase:

- Nonlinear effects: These items will be addressed in the later development phase.
  - Stimulated Raman scattering (SRS)
  - Stimulated Brillouin scattering (SBS)
  - Self-phase modulation (SPM)
- Damage mechanism and thermal effects: These items will be addressed in the later development phase, if necessary.
  - Self-focusing (Kerr effect)
  - Thermal lensing
  - Temperature effect on the laser physics (cross-section changes and lifetime change)
  - Thermo-mechanical stress and its effect on the guided modes

Table 3.3 summarizes the various physics of PG fiber amplifier, considered or ignored in the present modeling. We will describe the details of the modeling in the following sections.

3.1.5 Details of modeling

3.1.5.1 Pointwise dynamics of inverted population

We start with the spatial pointwise dynamics of the active ions in the core. The Yb^{3+} ion has only two energy states: $^2F_{5/2}$ as the upper energy level and $^2F_{7/2}$ as the lower energy level. Those two energy levels are Stark split due to the surrounding host and randomized dipole polarization. Particularly the $^2F_{5/2}$ level has three distinguished Stark split level whereas $^2F_{7/2}$ has four Stark split levels. Therefore, there are multiple ways of absorbing and emitting photons with various energies. The line strength of these transitions depends on host material (i.e., the level of Stark splitting) and temperature. The line broadening mechanism is dominantly homogenous. This is due to the fact that the thermal population stabilization in each energy level is very fast, compared to the absorbing or radiating transition time. Therefore, the majority of ion population in each energy level occupies the lowest stark split level in the band. Hence, any transition from the lowest stark split level reduces the transition from the same energy level to other energy level.

	Physics
Included	Multiple transverse mode
	Spectrally resolved pump and signal light
	Spontaneous emission
	Partial derivative (time and space)
Ignored	Radiation (bending) loss
	Mode mixing
	Dispersion (including polarization dispersion)
	Stimulated Rayleigh scattering
	Response time of atomic energy state transition
Will be considered in the future	SRS
	SBS
	SPM
	Self focusing (Kerr)
	Thermal lensing
	Temperature effect on cross-sections and lifetime
	Thermo-mechanical effect

Table 2.3 Summary of modeled, ignored, and planned physics of phosphate glass fiber amplifier.

The pulse duration, which we are concerned about, is a few nanosecond long and it is significantly longer than the stabilization of energy level transition (inverse of the Rabi frequency and the damping). Hence, we can safely assume instantaneous stimulated energy transition from one energy level to the other [15].

Consider the density of excited ions n_2 and the density of ground state ions n_1. The change of n_2 can be modeled as [16]

$$\frac{dn_2}{dt} = \int_\lambda [\sigma_a(\lambda) n_1 - \sigma_e(\lambda) n_2] I(\vec{r}, t, \lambda) \frac{hc}{\lambda} d\lambda - \frac{n_2}{\tau}, \tag{3.5}$$

where σ_a, σ_e are the absorption and the emission cross-sections, $I(\vec{r}, t, \lambda)$ represents the intensity of light at position $\vec{r} = (x, y, z)$ and time t within the spectral bin $[\lambda, d\lambda + \Delta\lambda]$, h is the Planck's constant, c is the speed of light in vacuum, and τ is the decay time (lifetime) of the excited ions. The light intensity satisfies the following equation by definition

$$\int_\lambda I(\vec{r}, t, \lambda) d\lambda = I(\vec{r}, t), \tag{3.6}$$

where $I(\vec{r}, t)$ represents the conventional light intensity with a unit [W/m^2]. Also, as a trivial result from the definition, the following should hold at any time and any spatial coordinate.

$$n_1 + n_2 = 1. \tag{3.7}$$

Equation (3.5) models the change of excited ion density as a sum of the contributions from the stimulated absorption, the stimulated emission, and the spontaneous emission. Please note that in equation (3.5) n_2 and $n_1$are functions of time and space. We will consider the inverted population as a function of time and space throughout the entire manuscript. It is against a convention where one considers a spatially averaged inverted population and calculates the gain or loss of the signal in spatially averaged sense. In multimode fibers, it is more accurate to consider the pointwise dynamics of inverted population instead of the averaged inversion.

3.1.5.2 Pointwise dynamics of light intensity

Likewise we now consider a pointwise intensity of light and its dynamics, instead of averaging out through the transversal plane of propagation. This can be accomplished through the following procedure: Consider the guided modes and their electrical field distribution $E_i(r, \phi)$. Then, the electrical field of the multimode light can be represented through a superposition of each orthogonal transverse mode as

$$E(\vec{r}, t, \lambda) = \sum_i^N c_i(z, t, \lambda) E_i(r, \phi) \exp(i\omega t - i\beta_i z), \tag{3.8}$$

where c_i are complex weights, $\omega = 2\pi c/\lambda$ is the angular optical frequency, β_i is the propagation constant (eigenvalue of the Helmholtz equation) associated with the transverse mode i. Then the (time averaged) intensity of the light is obtained through the product of E and its complex conjugate, and by time averaging over the several cycles of optical frequency. In this procedure,

we notice that the cross terms beating with the spatial beating frequency of $\beta_i - \alpha_j$ can be ignored, if the linewidth of the laser light is broad enough. Then, we obtain

$$I(\vec{r},t,\lambda) = \frac{1}{T}\int_T E^*(\vec{r},t,\lambda)E^*(\vec{r},t,\lambda)\,dt = \sum_i^N C_i(z,t,\lambda)I_i(r,\phi), \tag{3.9}$$

where T is several optical cycles long time, $C_i = c_i c_i^*$ is the new intensity weight associated with ith transversal mode, and I_i is the intensity distribution of i^{th} transversal mode, normalized in the sense

$$\int_0^{2\pi}\int_0^{\infty} I_i(r,\phi)r\,dr\,d\phi = 1. \tag{3.10}$$

Next, we proceed to the propagation equation. Consider the propagation of one transverse mode. We can represent the light intensity I as $I(\vec{r},t,\lambda) = C_i(z,t,\lambda)I_i(r,\phi)$. The pointwise interaction between the light and the ion populations can be modeled as the Helmholtz equation with a source term. By introducing the transversal mode, we can reduce the Helmholtz equation into one-dimensional continuity equation. In this procedure, we also assume the slowly varying envelope approximation. Then, the resulting one-dimensional intensity propagation equation is [17, 18]

$$\frac{n}{c}\frac{\partial I^{\pm}(\vec{r},t,\lambda)}{\partial t} \pm \frac{\partial I^{\pm}(\vec{r},t,\lambda)}{\partial z} = -N_0[\sigma_e(\lambda)n_2 - \sigma_a(\lambda)n_1]I^{\pm}(\vec{r},t,\lambda) + I_s, \tag{3.11}$$

where n is the refractive index of the material, $I^{\pm}$ represents the propagating light intensity in the positive and the negative z direction, respectively, N_0 is the doping density of the active ions and I_s is the contribution from the spontaneous emission. Please note that we modeled both the forward and the backward propagating light. And the light includes all of the signal, ASE, and the pump lights. Please note that equation (3.11) has the source term on the right hand side, which is comprised of the contributions from the stimulated emission, the stimulated absorption, and the spontaneous emission.

We now replace $I^{\pm}$ with $C_i^{\pm}I_i$ and integrate the above equation in the transversal plane. Then, we have

$$\frac{n}{c}\frac{\partial C_i^{\pm}(z,t,\lambda)}{\partial t} \pm \frac{\partial C_i^{\pm}(z,t,\lambda)}{\partial z} = C_i^{\pm}(z,t,\lambda)\int_0^{2\pi}\int_0^{\infty} N_0[n_2\sigma_e(mbda) - n_1\sigma_a(\lambda)]I_i(r,\phi)r\,dr\,d\phi + \int_0^{2\pi}\int_0^{\infty} I_s(r,\phi)r\,dr\,d\phi. \tag{3.12}$$

In equation (3.12), the first integrating term in the right hand side indicates the gain or loss from the spatial distribution of the excited ion density and the ground state ion density. Hence, the gain coefficient α_i for the ith transversal mode can be defined as

$$\alpha_i(z,t,\lambda) \equiv \int_0^{2\pi}\int_0^{\infty} N_0\left[n_2\sigma_e(\lambda) - n_1\sigma_a(\lambda)\right]I_i(r,\phi)\,r\,dr\,d\phi. \tag{3.13}$$

The second integrating term in equation (3.12) represents the contribution from the spontaneous emission. The wavelength-integrated spontaneous emission for each mode, for an infinitesimally small propagation distance Δz, can be modeled as the following equation

$$P_{spon} = \left(\frac{\#spontaneousphotons}{sec}\right)(photonenergy)(capturefraction)\left(\frac{1}{\#modes}\right), \tag{3.14}$$

where the first term on the right hand side is the photon emitting rate from the spontaneous emission, which is

$$\left(\frac{\#spontaneousphotons}{sec}\right) = \frac{N_0 A\Delta z\int_0^{2\pi}\int_0^{\infty} n_2\,r\,dr\,d\phi}{\tau}, \tag{3.15}$$

where τ represents the lifetime of the excited state ions. The photon energy is given as hc/λ and the capture fraction of the entire core waveguide in either the positive z or the negative z direction can be approximated as the solid angle of the waveguide, which is $\pi\theta_c^2/4\pi$ where θ_c is the total internal reflection angle of the core/cladding boundary. Then, for a weakly guided core, we can approximate the capture fraction as $\Delta n/2n$, where Δn is the difference of the refractive indices between the core and the cladding.
On the other hand, the number of modes in multimode fiber is given as

$$\#modes \propto \frac{V^2}{2} = \frac{4\pi^2 r_{co}^2 n_1\Delta n}{\lambda^2} = \frac{4\pi A_{co} n_1\Delta n}{\lambda^2}, \tag{3.16}$$

where r_{co} is the core radius and A_{co} is the core area. Hence, the spontaneous emission power can be represented through

$$P_{spon} = \frac{N_0 hc\lambda}{8\pi n^2\tau}\left[\frac{1}{A_{co}\int_0^{2\pi}\int_0^{\infty} n_2\,r\,dr\,d\phi}\right]\Delta z, \tag{3.17}$$

where N is the number of modes. Since we want to divide the contribution of the spontaneous emission into the wavelength bin of $[\lambda, \lambda+\Delta\lambda]$, we utilize the well-known relationship between the lifetime and the emission cross-section [19]

$$\frac{1}{\tau} = 8\pi n^2 c\int_{\lambda}\frac{\sigma_e(\lambda)}{\lambda^4}\,d\lambda, \tag{3.18}$$

Please also note that such spontaneous emission has contribution to two orthogonal polarization states. Using these results, we can express the second term on the right hand side of equation (3.12) as

$$\int_0^{2\pi}\int_0^{\infty} I_s(r,\phi)\,r\,dr\,d\phi = \frac{2N_0hc^2\sigma_e(\lambda)}{\lambda^3}\left[\frac{1}{A_{co}\int_0^{2\pi}\int_0^{\infty} n_2\,r\,dr\,d\phi}\right], \tag{3.19}$$

where A_{co} represents the core area. Then, by combining the equation (3.12) and (3.19), we obtain the final propagation equation for the power $C_i^{\pm}$ for i^{th} transverse mode as

$$\frac{n}{c}\frac{\partial C_i^{\pm}(z,t,\lambda)}{\partial t} \pm \frac{\partial C_i^{\pm}(z,t,\lambda)}{\partial z} = \alpha_i(z,t,\lambda)C_i^{\pm}(z,t,\lambda) + \frac{2N_0hc^2\sigma_e(\lambda)}{\lambda^3}\left[\frac{1}{A_{co}}\int_0^{2\pi}\int_0^{\infty} n_2\,r\,dr\,d\phi\right]. \tag{3.20}$$

The above equation is the master equation to solve the positive and the negative propagating power for each transversal mode, for each spectral bin, as a function of time and position. The coupled partial differential equations of (3.5) and (3.12) form the governing equations to solve the amplifier dynamics. Please note that the intensity $I(\vec{r},t,\lambda)$ in equation (3.5) can be represented as

$$I(\vec{r},t,\lambda) = I_p(\vec{r},t,\lambda) + \sum_{i=1}^{N}\left[C_i^{+}(z,t,\lambda) + C_i^{-}(z,t,\lambda)\right] I_i(r,\phi), \tag{3.21}$$

where I_p represents the pump intensity. We treat the pump separately since the pump cannot be represented by the superposition of the core modes.

3.1.5.3 Pump propagation dynamics

The pump is guided in the inner cladding. In a perfectly circularly symmetric inner cladding, the pump light propagates as a superposition of many modes. Due to the different overlap between the doped core and each pump mode, the transverse pump profile changes as the pump propagates. Therefore, it would make a more accurate model to consider all the pump modes in a circularly symmetric inner cladding. However, when the inner-cladding is not circularly symmetric, the modes start mixing, eventually leading to rather a uniform intensity in a transversal cross-section of the inner-cladding. In this case of vigorous mode-mixing, we can safely assume a uniform pump intensity along the pump propagation.
For modeling of PG amplifier, we assume the uniform pump intensity in transversal plane. In other words, we assume an immediate pump intensity redistribution where the pump intensity immediately recovers the state of uniform transversal intensity profile. In this case, the pump propagation can be modeled collectively. For this we integrate equation (3.11) in the transverse

plane and average the intensity. In doing so, we integrate the entire transverse plane for the inner cladding. Then, we obtain the following.

$$\frac{n}{c}\frac{\partial I_p^{\pm}(z,t,\lambda)}{\partial t} \pm \frac{\partial I_p^{\pm}(z,t,\lambda)}{\partial z} = N_0\left[\frac{1}{A_{cl}}\int_0^{2\pi}\int_0^{\infty}[\sigma_e(\lambda)n_2 - \sigma_a(\lambda)n_1]r\,dr\,d\phi\right]I_p^{\pm}(z,t,\lambda) \quad (3.22)$$

where A_{cl} represents the inner cladding area. Please note that in the above equation, we ignored the spontaneous emission of the pump photons, since the effect will be negligible.

3.1.6 Cross-sections and lifetime

We have measured the fluorescence spectrum of a 5 wt % Yb_2O_3 doped PG fiber. We also measured the lifetime of the excited ions from the same fiber and found that $\tau = 1.44$ ms. From the measured fluorescence spectrum, we can calculate the emission cross-section spectrum using the Füchtbauer-Ladenburg equation [20]

$$\sigma_e(\lambda) = \frac{\lambda^4}{8\pi cn^2\tau}\frac{I_f(\lambda)}{\int_\lambda I_f(\lambda)d\lambda} \quad (3.23)$$

where I_f represents the measured fluorescence spectral intensity. Once we obtained the emission cross-section spectrum, we could calculate the absorption cross-section through the McCumber relation [16]

$$\sigma_a(\lambda) = \sigma_e(\lambda)\exp\left[\frac{hc}{kT}\left(\frac{1}{\lambda}-\frac{1}{\lambda_c}\right)\right], \quad (3.24)$$

where k is the Boltzmann constant, T is the temperature, and λ_c is the wavelength of crossing between the absorption and the emission cross-section. In PG Yb-doped fiber, it is known that the crossing wavelength is around at 976 nm. Through this process, we could obtain the emission and the absorption cross-section spectra as shown in figure 3.3. It is noteworthy that the emission cross-section of the Yb^{3+}-doped PG has the second peak at 1005 nm, which is different from conventional 1030 nm peak from silicate or FS glass host. Also another notable characteristic can be found in the absorption cross-section. The usual secondary peak around at 910 nm from silicate or FS host is not prominent in the PG host.

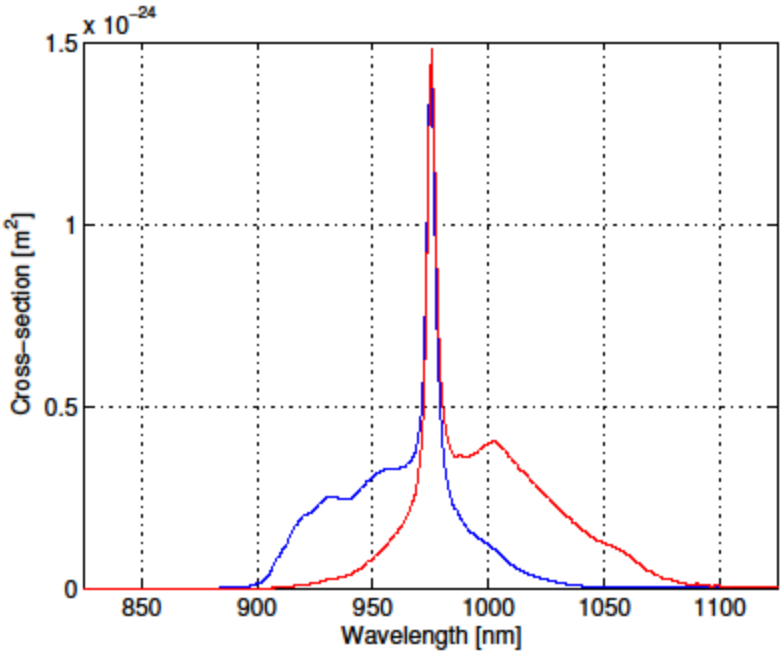

Figure 2.3 Measured emission (red) and absorption (blue) cross-section of 5 wt % Yb_2O_3 doped phosphate glass fiber.

3.1.7 Transverse modes and their behavior

It is of great concern how the mode will look in practical multimode fibers. Suppose an ideally circularly symmetric fiber. Let us consider the LP_{11} mode, represented by

$$E_{11}(r,\phi) = b(r)\cos(\phi + \phi_0), \tag{3.25}$$

where $b(r)$ represents the superposition of Bessel functions and ϕ_0 represents an angle off-set from the x-axis. The field represented by the above equation addresses an LP_{11} mode with two distinct lobes, with an angle ϕ_0 against the x-axis. Please note that one can expand the cosine term into $\cos(\phi + \phi_0) = \cos(\phi)\cos(\phi_0) - \sin(\phi)\sin(\phi_0)$, which is a superposition of the two orthogonal sine and cosine modes of the LP_{11} mode. Thus, it is apparent that any angle rotation can be represented by a superposition of the sine and the cosine orthogonal modes.
Now suppose that there is no differentiating element between the x- and the y-axis. This renders it rather ambiguous to distinguish the x- and the y-axis. In this scenario, a big question would be whether the ASE in LP_{11} mode will look like the canonical mode with the two distinct lobes. In order to tackle the problem in a more tractable way, we divide the situation into two stages. In the first stage, we can think of a situation where the photons are just captured by the modes. Some of the photons will be coupled into a certain LP_{11} mode with a particular angle ϕ_0. Each angle ϕ_0 will have the same chance to capture the photon since the probability for a photon to be created in a certain angle of radiance at a certain position will be uniform in the entire space. In the case of very large number of photon generation, it is plausible to think that there may arise all LP_{11} modes with all angles ϕ_0 equally. Especially, at this stage of mode creation, it would be

rather unreasonable to think that some angle will be dominant. Therefore, it appears to be reasonable to think that all the angles will arise equally in the mode forming stage. The next stage is the amplification. The LP_{11} modes with each different angle will have the same gain, provided that the initial spatial distribution of the inverted population is circularly symmetric. Then, it is also very natural to think that all the LP_{11} modes with various angles will be equally amplified, eventually leading to circularly symmetric inverted population. Therefore, in this picture, it is very likely that we will have a circularly symmetric LP_{11} mode, rather than a single LP_{11} mode with a certain angle ϕ_0.

On the other hand, suppose there is a differentiating element that clearly distinguishes the x- and the y-axis. In this scenario, the first mode formation stage will see the different rise of LP_{11} modes with different angle ϕ_0. Once the initial power associated with the variously angled LP_{11} is different, some mode will be quickly amplified in the second stage, becoming the dominant mode. Therefore, in this scenario, it is very natural to think of two distinct LP_{11} modes, namely the sine and cosine LP_{11} modes. This scenario is more likely in practical fiber lasers and amplifiers since the fiber is always bent. Once it is bent, clearly there exists preferred angle ϕ_0 to capture the photon from spontaneous emission. Also the same differentiating factor will discriminate the gain for different angled LP_{11} modes. Thus, it is very likely that in such case, one would see a very clear circularly asymmetric LP_{11} mode with two lobes (or combination of sine and cosine modes, thus four lobes). The same applies to the polarization-maintaining (PM) fiber, which has clearly different geometry for the distinguishable x- and y-axis.

The simulation results of a multimode fiber laser in reference [21] is noteworthy. In this study, the LP_{11} modes are treated as circularly symmetric mode. When the pump light started the laser process, the output signal has the largest portion in LP_{11} mode, which has double the power than LP_{01} mode. On the contrary, in another study, when the angular distribution is considered (i.e., the LP_{01} mode is not treated as circularly symmetric mode), the laser cavity produced the largest power in LP_{01} mode [22]. The same reference reports that the largest power was measured in the LP_{01} mode in an experiment. Please note that in the real experiment, the fiber was bent, which produced a clear distinction between the x-axis along the bending plane and the other axis. This also supports the argument that in real situation where there exists a clearly distinguishing element for x- and y-axis, the mode needs to be treated as sine and cosine modes, instead of the circularly symmetric mode.

The remaining question would be which scenario our PG fiber amplifier will belong to. Since the fiber is short and, thus, can be straight, it might be possible that our PG amplifier may generate donut-shaped LP_{11} modes. However, when the initial launching somehow preferred one angle, it may eventually generate a stronger power at a certain angle ϕ_0. Therefore, it is an open question, which can be verified only by experiment. Please note that the same argument applies to all the non-circularly symmetric higher modes such as LP_{12}, LP_{13}, LP_{21}, and so forth.

In either case, the mode intensities will be treated in normalized fashion. The modes are normalized in the sense that the transversal plane integral will produce 1. Mathematically, the mode intensities will have

$$\int_0^{2\pi}\int_0^{\infty} I_i(r,\phi) r\,dr\,d\phi = 1, \tag{3.26}$$

for each mode. If we need to treat the non-circular mode as a circularly symmetric mode, we will impose the following normalization,

$$2\pi \int_0^{\infty} I_i(r,0) r \, dr = 1, \tag{3.27}$$

where we will use the cosine mode for I_i distribution.
Figure 3.4 shows the normalized circularly symmetric mode intensities for the Fiber 1, which has 35 μm core diameter with 0.07 NA. The modal intensities are normalized in the sense of equation (3.27). Then, the number of modes reduces to eight from the original fifteen since we consider only the cosine modes.

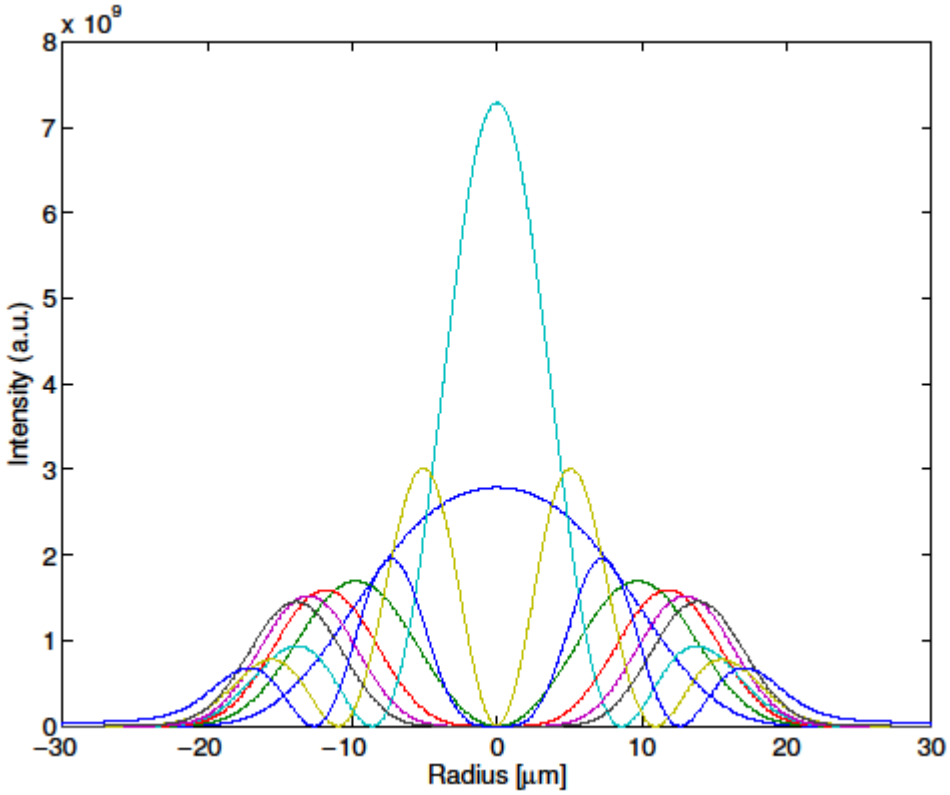

Figure 2.4 Circularly symmetrized and normalized mode intensity profiles of a step-index fiber with core diameter 35 μm and 0.07 NA, at 1005 nm.

3.2 Numerical simulator development

3.2.1 Introduction

In this chapter, we develop a numerical simulator for the pulsed amplification process in the PG Yb^{3+}-doped fiber. The numerical simulator will solve transient dynamics of the inverted population and the evolving power in each mode for both forward and the backward propagation directions. The numerical solution will be spectrally, temporally, and spatially resolved. The gain medium will be considered as a 3D object and the variables will be solved for each point in the three dimensional space, as a function of time. Therefore, the inverted population will be a 4D variable. The signal power will be resolved in modal numbers, instead of the [x,y] plane coordinates. Thus, the signal power will be a 4D variable (modal number, propagating distance, elapsed time, wavelength).
We have discussed the multimode behavior of the short straight fiber amplifier in section 3.1.7. We first approach the problem with circularly symmetric modes. Then, the dimension of the inverted population reduces to 3D since the inverted population will be also circularly symmetric and, thus, will be a function of radial position only in space.
The convergence and the simulation speed are both important goals to achieve. For this, we will implement the well-known numerical theorems that can be found in the textbook such as [23].

3.2.2 Theory for efficient numerical calculation

For clarity, the coupled differential equations to solve are repeated here.

$$\frac{dn_2}{dt} = \int_{\lambda} [\sigma_a(\lambda)n_1 - \sigma_e(\lambda)n_2]\, I(\vec{r},t,\lambda)\frac{\lambda}{hc}\mathrm{d}\lambda - \frac{n_2}{\tau}, \tag{3.28}$$

$$\frac{n}{c}\frac{\partial C_i^{\pm}(z,t,\lambda)}{\partial t} \pm \frac{\partial C_i^{\pm}(z,t,\lambda)}{\partial z} = \alpha_i(z,t,\lambda)C_i^{\pm}(z,t,\lambda) + \frac{2N_0hc^2\sigma_e(\alpha)}{\lambda^3}\left[\frac{1}{A_{co}\int_0^{2\pi}\int_0^{\infty} n_2\, r\,dr\,d\phi}\right], \tag{3.29}$$

where

$$I(\vec{r},t,\lambda) = I_p^{+}(z,t,\lambda) + I_p^{-}(z,t,\lambda) + \sum_{i=1}^{N}[C_i^{+}(z,t,\lambda) + C_i^{-}(z,t,\lambda)]\, I_i(r,\phi), \tag{3.30}$$

$$\alpha_i(z,t,\lambda) = \int_0^{2\pi}\int_0^{\infty} N_0\,[n_2\sigma_e(\lambda) - n_1\sigma_a(\lambda)]I_i(r,\phi)r\,dr\,d\phi. \tag{3.31}$$

And the pump propagation is given by

(3.32)

$$\frac{n}{c}\frac{\partial I_p^{\pm}(z,t,\lambda)}{\partial t} \pm \frac{\partial I_p^{\pm}(z,t,\lambda)}{\partial z} = N_0\left[\frac{1}{A_{ci}}\int_0^{2\pi}\int_0^{\infty}[\sigma_e(\lambda)n_2 - \sigma_a(\lambda)n_1]r\,dr\,d\phi\right]I_p^{\pm}(z,t,\lambda)$$

For the moment, we assume that the pump is in a pulsed mode, with a uniform power over the pumping duration. The seed signal is assumed to couple the input port after a steady-state inversion is reached through the constant pumping. In this scenario, in the time duration before the signal is launched into the amplifier, the inverted population will reach a steady state where the backward and the forward ASE is steadily generated.

3.2.2.1 Solving the steady-state boundary value problem

In a steady state without the seed signal, the above coupled partial differential equations are reduced to a set of steady-state time-invariant propagation equations. By setting the time derivative zero, we obtain the steady-state differential equation

$$\pm\frac{dC_i^{\pm}(z,\lambda)}{dz} = \alpha_i(z,\lambda)C_i^{\pm}(z,\lambda) + \frac{2N_0hc^2\sigma_e(\lambda)}{\lambda^3}\left[\frac{1}{A_{co}\int_0^{2\pi}\int_0^{\infty}n_2\,r\,dr\,d\phi}\right], \tag{3.33}$$

where the gain is still given by equation (3.31), but the inverted population is now represented by a static equation

$$n_2 = \frac{\int_{\lambda}\Gamma\sigma_a(\lambda)I(\vec{r},\lambda)\frac{\lambda}{hc}d\lambda}{1+\int_{\lambda}\Gamma[\sigma_a(\lambda)+\sigma_e(\lambda)]I(\vec{r},\lambda)\frac{\lambda}{hc}d\lambda}, \tag{3.34}$$

where I is still represented by equation (3.30), except for the time dependence. In addition, the pump propagation turns into a steady-state propagation equation given as

$$\pm\frac{dI_p^{\pm}(z,\lambda)}{dz} = N_0\left[\frac{1}{A_{ci}\int_0^{2\pi}\int_0^{\infty}[\sigma_e(\lambda)n_2 - \sigma_a(\lambda)n_1]\,r\,dr\,d\phi}\right]I_p^{\pm}(z,\lambda), \tag{3.35}$$

The corresponding boundary conditions are given by the fact that the forward signal power at the input (z=0) is all zero, regardless of modal number or wavelength, and the backward power at the output end ($z = L$, L is the amplifier fiber length) is all zero. These boundary conditions are mathematically

$$C_i^{+}(z=0,\lambda) = 0, \quad \forall\lambda, \quad \forall i \in [1,2,\cdots,N], \tag{3.36}$$

$$C_i^{-}(z=L,\lambda) = 0, \quad \forall\lambda, \quad \forall i \in [1,2,\cdots,N], \tag{3.37}$$

$$I_p^+(z=0,\lambda) = \frac{P_{p0}^+}{A_{cl}}\Lambda^+(\lambda), \tag{3.38}$$

$$I_p^-(z=L,\lambda) = \frac{P_{p0}^-}{A_{cl}}\Lambda^-(\lambda), \tag{3.39}$$

where $\Lambda^{\pm}(\lambda)$ represent the optical spectrum of the pump light with $\int_\lambda \Lambda^{\pm}(\lambda)d\lambda = 1$, P_{p0}^{+} represent the pump power in [W] for the forward and the backward pumps, and A_{cl} is the cladding area. Therefore, the system equation reduces to the ordinary differential equation in (3.33) with the boundary conditions in equation (3.36) to (3.39).

We adopt the shooting method as in [23] to solve the boundary value problem. Solving the problem means that we find out all $C_i^{\pm}(z,\lambda)$ for all i, for all z, and for all λ, as well as $I_p^{\pm}(z,\lambda)$ for all z and for all λ. However, the final goal is to find the steady-state distribution of the inverted population, utilizing the information of $C_i^{\pm}(z,\lambda)$, using the equation (3.34). In shooting method, the convergence of numerical solution hugely depends on the initial conditions. In our case, the initial conditions are $C_i^-(z=0,\lambda)$ for all i and for all λ, and $I_p^-(z=0,\lambda)$ for all λ, in case we integrate the differential equations (3.33) and (3.35) from $z=0$ to $z=L$. The goal is to match the boundary conditions given in (3.37) and (3.39). Thus, it is very important to start with a good initial condition set for $C_i^-(z=0,\lambda)$ and $I_p^-(z=0,\lambda)$.

In order to guess the suitable initial conditions for shooting method, we adopt an intelligent heuristic method. It has been known in the laser society, without rigorous proof, that one can obtain an initial condition set, which is very close to the final solution to the laser boundary value problem, through the following procedure.

1. With the initial condition set (3.38), integrate the pump differential equation in (3.35), in forward direction only (I_p^+), assuming that $n_2 = 0$ for all z and r.
2. Obtain $n_2(z,r)$ using equation (3.34), based on the obtained $I_p^+(z,\lambda)$.
3. With the initial condition set (3.37), integrate the signal differential equation in (3.33) in backward direction only (C_i^-), assuming the obtained $n_2(z,r)$.
4. With the initial condition set (3.39), integrate the pump differential equation in (3.35), in backward direction only (I_p^-), assuming the obtained $n_2(z,r)$.
5. Update $n_2(z,r)$ using equation (3.34), based on the obtained $I_p^{\pm}(z,\lambda)$ and $C_i(z,\lambda)$.
6. With the initial condition set (3.36), integrate the signal differential equation in (3.33) in forward direction only (C_i^+), assuming the obtained $n_2(z,r)$.
7. Update $n_2(z,r)$ using equation (3.34), based on the obtained $I_p^{\pm}(z,\lambda)$ and $C_i^{\pm}(z,\lambda)$.
8. Repeat the routine from 1 to 7, until $n_2(z,r)$ does not change through the updating process, which is equivalent to having found solutions to the differential equations of concern.

The above routine works very well in most cases of steady-state laser/amplifier problems. In many cases, the above routine find the solution almost exactly, without further need to implement the full blown shooting method routines. The only potential problem with the above

method is that it does not guarantee a global convergence, even if the differential equations are stable to perturbation (absolutely negative), whereas the shooting method with Newton-Raphson algorithm mathematically guarantees the global convergence of the numerical solution in the same differential equation.

For a mathematically sure convergence, we start with the initial conditions with reasonable accuracy, obtained through the above procedures. Then we apply the full blown shooting method as follows. Suppose that the unknown initial conditions to obtain are represented by a raw vector given by

$$V = \begin{bmatrix} C_1^-(z=0,\lambda_1) \\ \vdots \\ C_N^-(z=0,\lambda_1) \\ \hdashline \vdots \\ \hdashline C_1^-(z=0,\lambda_n) \\ \vdots \\ C_N^-(z=0,\lambda_n) \\ \hdashline L_p^-(z=0,\lambda_1) \\ \vdots \\ L_p^-(z-0,\lambda_n) \end{bmatrix}, \tag{3.40}$$

The error of trial solution on the boundary condition is then given by

$$F = \begin{bmatrix} C_1^-(z=L,\lambda_1) \\ \vdots \\ C_N^-(z=L,\lambda_1) \\ \hdashline \vdots \\ \hdashline C_1^-(z=L,\lambda_n) \\ \vdots \\ C_N^-(z=L,\lambda_n) \\ \hdashline L_p^-(z=L,\lambda_1) - \left(P_{p0}^-/A_{ct}\right)A(\lambda_1) \\ \vdots \\ L_p^-(z=L,\lambda_n) - \left(P_{p0}^-/A_{ct}\right)A(\lambda_n) \end{bmatrix}, \tag{3.41}$$

which is a raw vector, with the number of entry equal to $N_{mode} \times N_\lambda + N_\lambda$, where N_{mode} is the number of transversal guided modes in the core and N_λ is the number of wavelength bins. The purpose is to reduce the F to zero, which is equivalent to satisfing the boundary conditions (3.37) and (3.39). Then, we employ the Newton-Raphson root finding algorithm as follows: The next iterating initial condition $V^{(i+1)}$ is given by

$$V^{i+1} = V^i + \delta V, \tag{3.42}$$

where the adjusted difference δV is a solution to the following Jacobian equation

$$-J\ \delta V = F, \tag{3.43}$$

where the Jacobian J can be obtained by the following equation

$$J_{ij} = \frac{F_i(v_1, v_2, \cdots, v_i + \Delta v_j, \cdots) - F_i(v_1, v_2, \cdots, v_i, \cdots)}{\Delta v_j}, \tag{3.44}$$

where v_j are the elements of vector V and F_i are the elements of vector F. The equation (3.44) is numerically evaluated each time by perturbing the initial condition v_j with $v_j + \Delta v$ where Δv is a small number. Therefore, obtaining the Jacobian matrix J requires integrating the whole differential equations $(N_{mode+1}) \times N_\lambda$ times with different initial condition every time. Solving equation (3.43) requires that the Jacobian matrix J has an inverse matrix, which is guaranteed by the fact that the differential equation is perturbation-stable (absolutely negative).

The final criterion for convergence in mathematical terms can be defined as follows: Suppose that we impose an absolute tolerance ϵ_a, which is typically order of 10^{-6} smaller than the solution value, and a relative tolerance ϵ_r, which is typically order of 10^{-6}. Then, we can define a row vector

$$S \equiv \epsilon_a + \epsilon_r |V|. \tag{3.45}$$

The solution error is defined by

$$\varepsilon = \sqrt{\frac{1}{N_v} \sum_1^{N_v} \left(\frac{F_i}{S_i}\right)^2}, \tag{3.46}$$

where $N_v = N_{mode} \times N_\lambda$ and S_i are elements of the vector S. When ε is less than 1, we can accept the trial solution V as the converged solution.

Again it is often desired to avoid the full blown shooting procedure since one has to integrate $(N_{mode} + 1) \times N_\lambda$ times the differential equation for one iteration and it is quite often that the required number of iterations exceeds 10 or even 100. Therefore, overall one has to integrate the differential equation many times. Suppose that we have $N_{mode} = 9$ and $N_\lambda = 300$, which is a typical case for our problem. Then, one would integrate the differential equations 30,000 to 300,000 times in a full blown shooting algorithm, whereas the heuristic method above requires less than 30 times of integration, with a reasonably good accuracy. The heuristic result may be verified through the error convergence criterion (3.46). Therefore, a complete algorithm will start with the heuristic method for guessing a reasonable initial condition set, verifying the heuristic result obtained through the error criterion. The full blown shooting method is initiated only if the

heuristic method fails. With this procedure we achieve the efficiency and the accuracy at the same time.
One thing to note is that the heuristic method is very effective when one has a well-defined seed signal, which has a power level well above the saturating power of the amplifier. However, when there is no such well-defined seed signal, the heuristic method often fails, which necessitates the use of the full-blown shooting method. Unfortunately, in our case of PG amplifier, the steady-state solution we require does not have a well-defined input seed, which forces us to resort to the full-blown shooting method.

3.2.2.2 Solving the partial differential equation

Please recall that it is assumed that the signal pulse arrives after the steady-state is achieved. As a result of solving the steady-state equations, we now have the initial conditions at time $t = 0$. These are given in the following set of initial conditions.

$$C_i^{\pm}(z, t = 0, \lambda) = C_i^{\pm ss}(z, \lambda), \tag{3.47}$$

$$I_p^{\pm}(z, t = 0, \lambda) = I_p^{\pm ss}(z, \lambda), \tag{3.48}$$

$$n_2(z, t = 0, r) = n_2^{ss}(z, r), \tag{3.49}$$

where the superscript ‘ss’ represents ‘stead-state’.

Euler Method

The next task is to solve the partial differential equations shown in (3.2.1) and below, with the initial conditions given above. For this, we adopt the finite difference method as in [23]. The idea is to represent the partial differential equations into difference equations.

$$\left(\frac{n}{c}\right)\frac{C_i^{\pm}(z_f, t_{n+1}, \lambda) - C_i^{\pm}(z_f, t_n, \lambda)}{\Delta t} \pm \frac{C_i^{\pm}(z_{f+1}, t_n, \lambda) - C_i^{\pm}(z_{f-1}, t_n, \lambda)}{2\Delta z} = \alpha_i(z_f, t_n, \lambda) C_i^{\pm}(z_f, t_n, \lambda) + \frac{2N_0 hc^2 \sigma_e(\lambda)}{\lambda^3}\left[\frac{1}{A_{co}\int_0^{2\pi}\int_0^{\infty} n_2\, r\, dr\, d\phi}\right]_r \tag{3.50}$$

$$\left(\frac{n}{c}\right)\frac{I_p^{\pm}(z_f, t_{n+1}, \lambda) - I_p^{\pm}(z_f, t_n, \lambda)}{\Delta t} \pm \frac{I_p^{\pm}(z_{f+1}, t_n, \lambda) - I_p^{\pm}(z_{f-1}, t_n, \lambda)}{2\Delta z} = N_0\left[\frac{1}{A_{cl}}\int_0^{2\pi}\int_0^{\infty}\left[\sigma_e(\lambda) n_2(z_f, t_n, r) - \sigma_a(\lambda) n_1(z_f, t_n, r)\right] r\, dr\, d\phi\right] I_p^{\pm}(z_f, t_n, \lambda) \tag{3.51}$$

$$\frac{n_2(z_j,t_{n+1},r)-n_2(z_j,t_n,r)}{\Delta t} = \int_\lambda [\sigma_a(\lambda)n_1(z_j,t_n,r)-\sigma_e(\lambda)n_2(z_j,t_n,r)]I(\vec{r}_j,t_n,\lambda)\frac{\lambda}{hc}d\lambda - \frac{n_2(z_j,t_n,r)}{\tau} \quad (3.52)$$

where t_n represents the nth time bin and z_j represents the jth time bin. In the above equations, the relevant variables are defined as

$$\alpha_i(z_j,t_n,\lambda) = \int_0^{2\pi}\int_0^{\infty} N_0\left[n_2(z_j,t_n,r)\sigma_e(\lambda)-n_1(z_j,t_n,r)\sigma_a(\lambda)\right]I_i(r,\phi)r\,dr\,d\phi, \quad (3.53)$$

$$I(\vec{r}_j,t_n,\lambda) = I_p^+(z_j,t_n)+I_p^-(z_j,t_n)+\sum_{i=1}^{N}\left[C_i^+(z_j,t_n,\lambda)+C_i^-(z_j,t_n,\lambda)\right]I_i(r,\phi). \quad (3.54)$$

Please note that in the coupled partial differential equations (3.50), (3.51), and (3.52), we treated the inversion n_2 as a separate variable since it has its own dynamic. In addition, we adopted a forward derivative for the time derivative whereas a center derivative for the space derivative. The numerical accuracy of center derivative is higher than the forward derivative. The reason for the forward time derivative is clarified in the following explanation.

The finite difference equations enable us to obtain the variables at time t_{n+1} with the information at time t_n. Therefore, once we know the information $C_i^{\pm}(z_j,t_0,\lambda)$, $I_p^{\pm}(z_j,t_0,\lambda)$, and $n_2(z_j,t_0,r)$ for all z_j's, all λs, and all r, we can obtain $C_i^{\pm}(z_j,t_n,\lambda)$, $I_p^{\pm}(z_j,t_n,\lambda)$, and $n_2(z_j,t_n,r)$ for all z_j's, all λs, and all r, for all t_n's. Please also note that we have boundary condition to match:

$$C_i^+(z=0,t_n,\lambda) = P_{s0}^{i+}(t_n,\lambda), \quad \forall i, \quad \forall\lambda, \quad \forall t_n, \quad (3.55)$$

$$C_i^-(z=L,t_n,\lambda) = P_{s0}^{i-}(t_n,\lambda), \quad \forall i, \quad \forall\lambda, \quad \forall t_n, \quad (3.56)$$

$$I_p^+(z=0,t_n,\lambda) = \frac{P_{p0}^+}{A_{ci}}\Lambda^+(\lambda), \quad \forall t_n, \quad (3.57)$$

$$I_p^-(z=L,t_n,\lambda) = \frac{P_{p0}^-}{A_{ci}}\Lambda^-(\lambda), \quad \forall t_n, \quad (3.58)$$

where we will impose the signal coupling on any of $P_{s0}^{i\pm}(t_n,\lambda)$, depending on the direction of seed signal coupling. We also can vary the coupled power of seed signal into multiple transversal modes. The time dependent, wavelength dependent, initial power $P_{s0}^{i\pm}(t_n,\lambda)$ will fully address the variability of the coupled seed signal. For a trivial case, where there is no coupled seed power for particular i, t_n, and λ, we can set $P_{s0}^{i\pm}(t_n,\lambda)=0$. This will render the dynamic equation solver to solve the steady-state solution.

Lax modification

Unfortunately, however, due to the numerically unstable nature of the Euler method in equations (3.50) and below, as explained in reference [23], it is often necessary to implement the *Lax modification* for numerical stability. The Lax modification makes the following change:

$$\frac{C_i^{\pm}(z_f, t_{n+1}, \lambda) - C_i^{\pm}(z_f, t_n, \lambda)}{\Delta t} \rightarrow \frac{C_i^{\pm}(z_f, t_{n+1}, \lambda) - \frac{1}{2}\left(C_i^{\pm}(z_{f+1}, t_n, \lambda) + C_i^{\pm}(z_{f-1}, t_n, lambda)\right)}{\Delta t}, \tag{3.59}$$

$$\frac{I_p^{\pm}(z_f, t_{n+1}, \lambda) - I_p^{\pm}(z_f, t_n, \lambda)}{\Delta t} \rightarrow \frac{I_p^{\pm}(z_f, t_{n+1}, \lambda) - \frac{1}{2}\left(I_p^{\pm}(z_{f+1}, t_n, \lambda) + I_p^{\pm}(z_{f-1}, t_n, lambda)\right)}{\Delta t}, \tag{3.60}$$

$$\frac{n_2(z_f, t_{n+1}, \lambda) - n_2(z_f, t_n, \lambda)}{\Delta t} \rightarrow \frac{n_2(z_f, t_{n+1}, \lambda) - \frac{1}{2}\left(n_2(z_{f+1}, t_n, \lambda) + n_2(z_{f-1}, t_n, \lambda)\right)}{\Delta t}, \tag{3.61}$$

The above modification guarantees the *von Neuman numerical stability* [23]. Additionally, in order to completely satisfy the stability criterion, we need the *Courant condition* given by [23]

$$\left(\frac{c}{n}\right)\frac{\Delta t}{\Delta z} \leq 1. \tag{3.62}$$

Suppose that we will divide the z element into 100 bins when the amplifier length is 0.2 m. Then, the Courant condition requires that the time grid size Δt should be less than 10 ps.

Reduction of power propagation equation

In special cases where the fiber amplifier length is sufficiently short, the propagation time of the pulse inside the amplifier is negligible compared to other time scales. In mathematical terms such assumption is equivalent to ignoring the first term on the left hand side of equation (3.29). Then, the equation is reduced to one dimensional ordinary differential equation given as

$$\pm\frac{\partial C_i^{\pm}(z, t, \lambda)}{\partial z} = \alpha_i(z, t, \lambda) C_i^{\pm}(z, t, \lambda) + \frac{2N_0 hc^2 \sigma_e(\lambda)}{\lambda^3}\left[\frac{1}{A_{co}\int_0^{2\pi}\int_0^{\infty} n_2\, r\, dr d\phi}\right]. \tag{3.63}$$

This approximation reduces the computational burden a great amount. The above equation is in the form of

$$\frac{y(z)}{dz} = f_1(z)y(z) + f_0(z), \tag{3.64}$$

where f_1 and f_0 are arbitrary integrable function. The above equation has an analytical solution given by

$$y(z) = \exp\left[F(x)\right]\left\{y(0) + \int_0^z \exp\left[F(z')\right] f_0(z')\,dz\right\}, \tag{3.65}$$

where

$$F(z) = \int_0^z f_1(z')\,dz. \tag{3.66}$$

The only remaining partial time derivative is on the inversion equation in (3.28). The strategy to solving these reduced equations is to solve the reduced ordinary differential equation (3.63) with the boundary condition given by (3.59) and below, for given inversion n_2 at time t_n. Then, one can obtain n_2 at t_{n+1}, using the partial differential equation in (3.28).

Upwind and downwind combo method

Although the reduction method might produce a reasonably credible result, still the consequences of ignoring the time derivative are uncertain. Therefore, it is logical to have a comprehensive simulator to compare with. Once we have a comprehensive simulator that does not compromise the model and produces a reliable result, we can judge whether the approximations we made are reasonable or not. For this, we revisit the full partial equation and seek a method to solve it.

Although the Lax modification may produce numerically stable result, whether to adopt the method is subject to the availability of suitable boundary conditions. Suppose a simple partial differential equation

$$u_t + v u_x = f(t, x), \tag{3.67}$$

where u_t and u_x represent the time and the spatial derivatives, respectively, v is a constant, and f is an arbitrary integrable function. There are many ways of finite difference schemes to solve the partial differential equation. These include (1) Euler method, (2) LAX modification, (3) upwind, (4) downwind, (5) Lax-Wendroff, (6) leapfrog, which are explicit methods, and (7) Crank-Nicolson and (8) box methods which are implicit[1].

We tested each method extensively. As we have discussed earlier, the Euler method would not produce numerically stable result. All other methods except for the upwind/downwind methods, diverged. In order to explain the reason, let us look into the Lax modification. The modified difference equation in Lax scheme is

$$u_j^{n+1} = \frac{1}{2}\left(u_{j+1}^n + u_{j-1}^n\right) + \Delta t\left[-v\,\frac{u_{j+1}^n - u_{j-1}^n}{2\Delta x} + f(n\Delta t, j\Delta x)\right]. \tag{3.68}$$

[1]For further details of each method, please see 24. Thomas, J.W., *Numerical partial differential equations - finite differences methods.* New York: Springer-Verlag, 1995..

This equation should be solved for each $j - 1,2, \dots, J$. Then, it is apparent that one needs a boundary condition both at $j = 1$ and $j = J$ for all $n = 1,2, \dots, N$. Therefore, it is clear that the Lax method can be used only when one knows the boundary values u_1^n and u_J^n for all n. The same is true to all the methods that diverged. However, our boundary conditions given in (3.55) and below has alternating boundary conditions. That is, for forward signal and pump we have boundary conditions at $z = 0$ and for backward signal and pump we have boundary conditions at $z = L$. It is mathematically trivial to see that the Lax equation in (3.68) will produce a wrong result unless both boundary values are known exactly.

A natural idea is to use the upwind method for the backward signal and the backward pump. In the upwind method, the partial differential equation is posed as

$$u_j^{n+1} = u_j^n + \Delta t \left[-v \frac{u_{j+1}^n - u_j^n}{\Delta x} + f(n\Delta t, j\Delta x) \right]. \tag{3.69}$$

With this calculation procedure, one can obtain u_{j-1}^{n+1} from u_j^n and u_{j-1}^n. With recursive application, one would obtain all the $u_{j-1}^{n+1}, u_{j-2}^{n+1}, \dots, u_1^{n+1}$ while u_j^{n+1} is directly given from the boundary condition. Therefore, we obtain all the values at time $t = (n+1)\Delta t$ without ambiguity. On the other hand, for the forward signal and pump, we can use the downwind method, represented by

$$u_j^{n+1} = u_j^n + \Delta t \left[-v \frac{u_j^n - u_{j-1}^n}{\Delta x} + f(n\Delta t, j\Delta x) \right]. \tag{3.70}$$

In a similar manner, we obtain u_2^{n+1} from u_1^n and u_2^n. With recursive application of the above equation, one obtains $u_2^{n+1}, u_3^{n+1}, \dots, u_J^{n+1}$ while u_1^{n+1} is directly obtained from the boundary condition.

With this combined method, we can numerically solve the full partial differential equation without any ambiguity. One disadvantage of this method is the error order, which is $O(\Delta x)$ in this case since it uses the forward or the backward differences, instead of the central difference which has $O(\Delta x^2)$. Therefore, it is expected that the grids will be finer with this upwind and downwind combo method, in order to produce reliable result. However, please note that it is much better to sacrifice the simulation time than not to be able to obtain accurate result at all.

3.2.3 Numerical simulator

We developed a numerical simulator to solve the partial differential equation. It is based on the Matlab programming language. Since the partial differential equation involves many dimensional tensors and their multiplications, Matlab is one of the most efficient tools to solve such large dimensional variables. The developed numerical simulator has three parts:

1. The simulator solves the transversal modes for the given fiber geometry.
2. It solves the steady-state condition with the given pump powers in both forward and backward directions, assuming no input signal.
3. It then solves the full partial differential equation.

The first step takes only several seconds with a good accuracy. This is remarkable in that, using other tools, obtaining the eigenvalues and eigenfunctions from the Helmholtz equation typically takes many minutes. Such calculation efficiency was accomplished by optimizing the Matlab code.

3.2.3.1 Steady-state solution

The second step is divided into two sub-steps: firstly, the simulator obtains a reasonable initial guess for the steady-state solution by the heuristic method described in the previous section 3.2.2.1. Once a good initial condition is obtained, the simulator solves the steady-state using a full-blown shooting method. In this latter step, obtaining the Jacobian matrix for Newton-Raphson updating rule is a completely parallel job, which can be divided into multiple independent calculating cores. This reduces the simulation time to a great extent. As a result, a full-blown shooting method to obtain the modal power resolved, 3-D spatially resolved, and wavelength resolved steady-state solution takes less than a minute[2]. In solving the steady-state solution, the absolute and the relative accuracy ϵ_a and ϵ_r are both set to 10^{-10}. Also it is noteworthy that the Newton-Raphson updating rule is in practice used as

$$\delta V = -\kappa J^{-1} F, \tag{3.71}$$

where κ is set to 0.5. When κ is set to 1, the Newton-Raphson iteration may diverge, especially in case where the *attracting region in parameter space* is small. Thus, reducing the speed of update often induces additional numerical stability.
For a sanity check of the developed numerical simulator, we can compare with published results. We picked the reference [25]. It is based on a germanosilicate Yb-doped fiber whose spectroscopic data is taken from another reference [26]. In fact, reference [27] decomposed the emission and the absorption cross-section spectra of the germanosiliate Yb^{3+}-doped fiber into superpositions of four Gaussian envelopes with different heights and different center

[2]This compares well with my previous code, which was built back in 2004, for similar purposes. The old code took approximately an hour to obtain the same result. Part of the reason is ascribed to the faster CPU clock, which is a factor of 1.5. Thus, the majority of improve came from parallel computing and code optimization.

wavelengths. The spectroscopy from the same reference is rebuilt and shown in figure 3.5. The other parameter used in the calculations are summarized in the table 3.4.

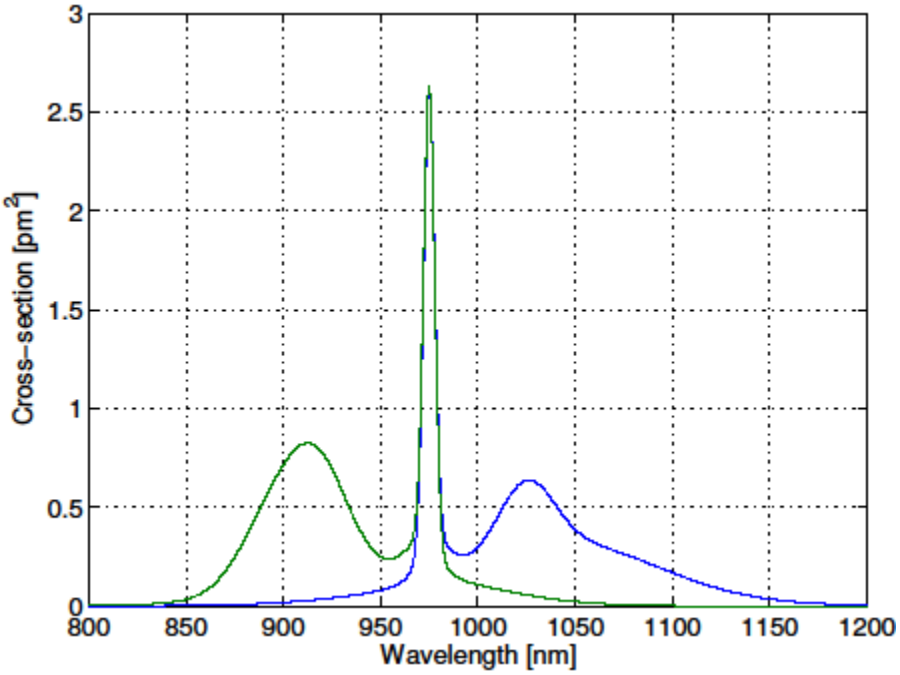

Figure 2.5 The emission (blue) and the absorption (green) cross-section spectra of germanosilicate Yb-doped fiber (reconstructed from [26].)

Parameter	Value	Parameter	Value
Pump wavelength	915 nm	τ	840 s
Signal wavelength	1064 nm	L	10 m
Core radius	9.8 μm	Core NA	0.07
Cladding radius	98 μm	Pump power (forward)	20 W
N_0	6×10^{25}	Pump power (backward)	0 W

Table 2.4 Parameter used for sanity check of the numerical simulator.

There are seven guided modes in this fiber at 1064 nm. For simplicity, we ignored all the other transverse modes, except for the fundamental LP_{01} mode as in the reference [25].
Solving the steady-state equation took 20 seconds. The converged solution had very similar result as in reference [25]. Figure 3.6 shows the obtained steady-state inversion at the center of the core, with 20 W forward pump power and no signal injected yet. Figure 3.7 shows the power of the forward pump, the forward signal, and the backward signal power. The same figure also shows the output ASE spectra. The slight difference between the result in reference [25] and the results presented here is ascribed to the fact that the emission and the absorption cross-section in reference [25] is in fact slightly different from the reference [26], although the reference claims that it took the same spectroscopy data from the same reference. Nevertheless, there is a sufficient level of similarities among the obtained result, which assures the accuracy of the steady-state solver.

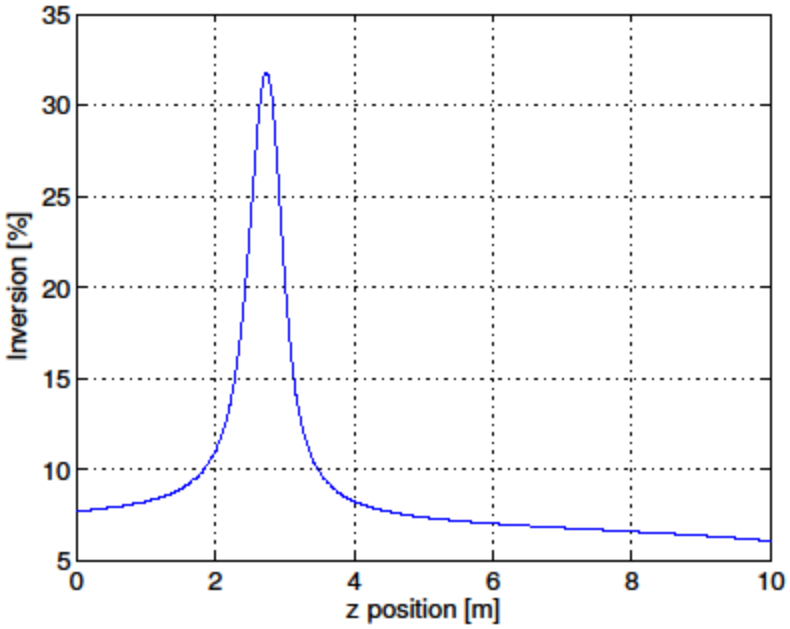

Figure 2.6 Steady-state inversion at the center of core.

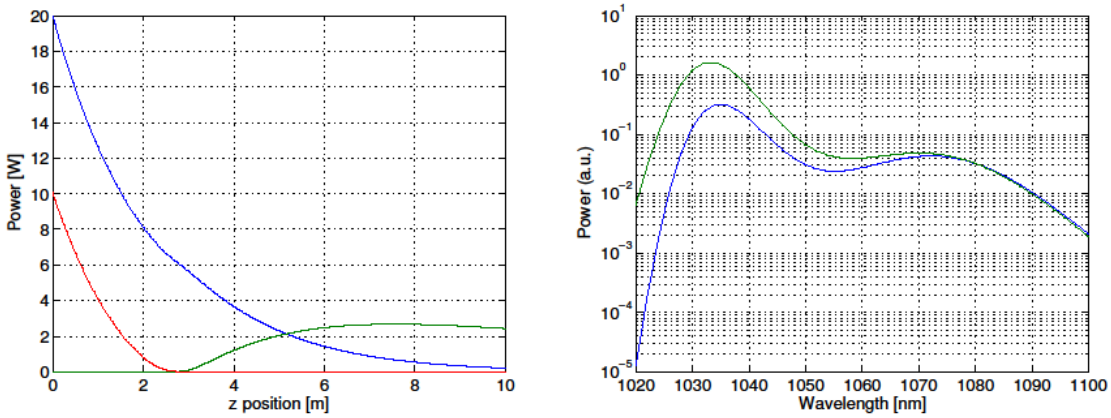

(a) Power (b) Output ASE spectra

Figure 2.7 Obtained steady state power evolution and output ASE spectra. Left: blue - forward pump, red - backward ASE, green - forward ASE. Right: green - backward ASE, blue - forward ASE.

3.2.3.2 Transient solution

As we obtained the steady-state solution before the signal is injected, we are now ready to solve the transient response of the amplifier when a pulsed signal is injected. Before going too further, we checked the sanity of the developed numerical partial differential equation solver. A good way to check the sanity might be to see that the transient partial differential equation solver will not alter the steady-state solution obtained previously, in case the signal is not injected. If the

transient solver alters the steady-state solution, it is evidence that the transient solver is not operating properly.

Euler method

We first try the method as in equation (3.50). This is the most primitive and simple finite difference method. For the calculation, we assume time steps Δt of 50 ps and spatial steps Δz of 5 cm, which certainly satisfies the Courant condition.
When we coded with this simple method, we experienced numerical instability, which eventually lead to divergence. Figure 3.8 shows the result when we ran only for 6.5 ns with the initial condition same as the steady-state solution. For the first 4 ns, the steady-state is preserved at an inversion distribution along z direction similar to the initial condition. However, after 4 ns, a spurious noise arises, which eventually leads to pathological divergence located at 5 m and 6 ns. Thus, we conclude that the simple finite difference method does not work for our nonlinear partial differential equation.

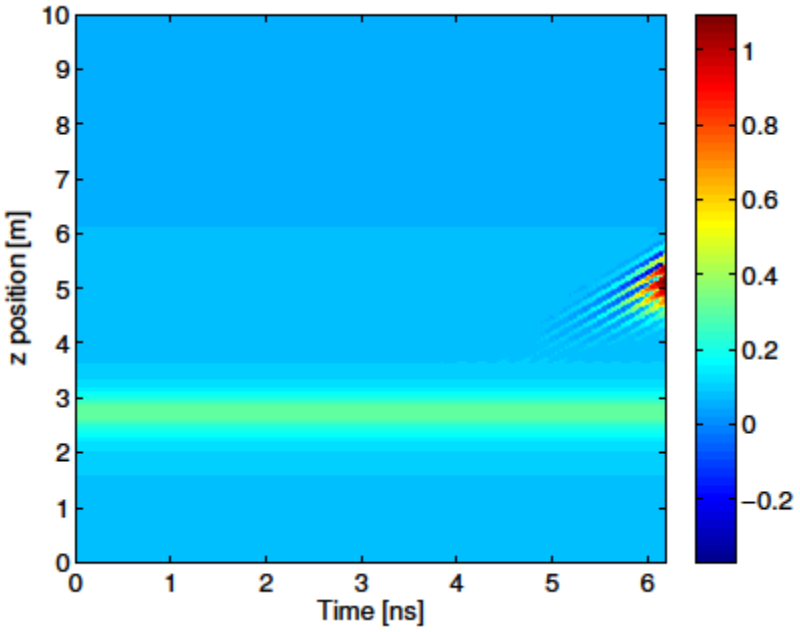

Figure 2.8 Obtained inversion as function of time t and space z, based on simple finite difference method.

Lax modification

Next, we adopted the Lax modification, which induces a numerical damping term as in equation (3.59). The result is shown in figure 3.9. The inversion shows a significant change as time elapses. Although we did not observe any numerical instability, the initially concentrated inversion at position 2.8 m is gradually dissipated throughout the entire space. Clearly the Lax modification did not preserve the steady-state solution. A partial explanation can be seen from

the lax modification itself, where $C_i(z_j, t_{n+1})$ is affected by the averaged value between $C_i(z_{j+1}, t_n)$ and $C_i(z_{j-1}, t_n)$. This eventually leads to the diffusion-like phenomenon shown in the figure 3.9.

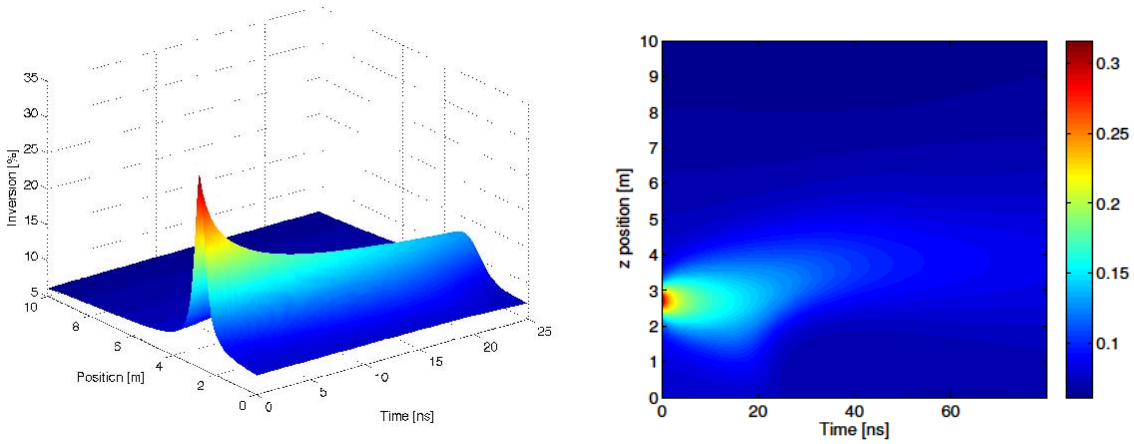

Figure 2.9 Obtained inversion as function of time t and space z, based on Lax modification.

Reduction of propagation equation

Next, we adopted the reduction method, explained in section 9.2.3. Now, we obtained a reasonable result as shown in figure 3.10. It is observed that the inversion is perfectly preserved throughout the entire of time of simulation. This implies that the steady-state solution is preserved in this partial differential equation solver, which is a strong indication that the solver operates properly.

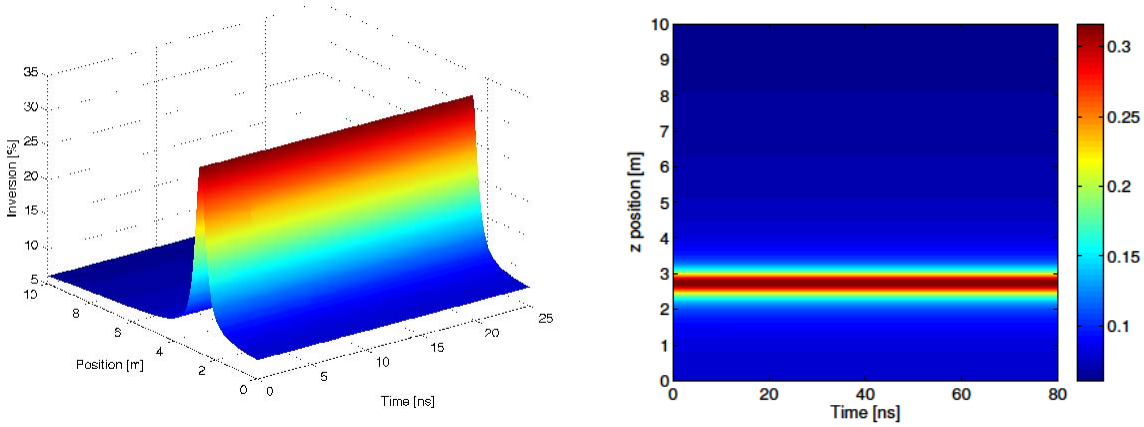

Figure 2.10 Obtained inversion as function of time and space, based on reduction method.

As we are ready to test the dynamics when the seed pulse is injected, we injected an input signal pulse at 1064 nm with 1 μJ pulse energy and 20 ns pulse duration (FWHM). Now that the input

is no longer time-invariant, we would see a dynamic change in the population inversion and the output power in both backward and forward directions. Figure 3.11 shows the forward output power as a function of time. The obtained pulse trace and the energy is very similar to the result in [25]. We observed that the output pulse experiences a serious saturation effect in the front part so that the pulse after 18 ns is no longer amplified although the instantaneous power of the input pulse is still increasing. The temporal shape of the output pulse clearly shows the pulse energy saturation of the amplifier.

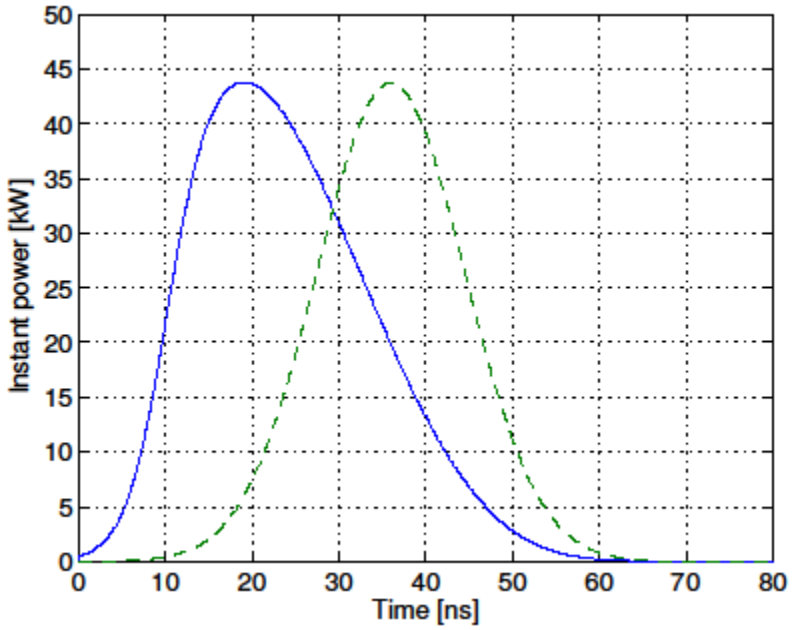

Figure 2.11 Output power time trace (blue) when 20 ns input pulse with 1 μJ at 1064 nm is injected (green). Please note that the input pulse is exaggerated by a factor of 930, in order to be compared easily with the output pulse.

Such pulse energy saturation is clearly seen through the inversion as shown in figure 3.12. The inverted population begins to be depleted significantly after 18 ns. Then, after 40 ns the inversion is depleted significantly. The difference in the inversion between the 40 ns and the initial condition is now transferred to the output pulse energy. Please also note that the inversion between 3 m and 10 m are also depleted, changing the color from light blue to dark blue. Such inversion depletion starts from far end at 10 m and gradually backward-propagates towards the 3 m position. This indicates that the saturation intensity is reached firstly at the 10 m region in the beginning phase where the input pulse's instant power is low. As the time passes and the input pulse instant power increases, such saturating intensity is reached at closer positions towards to the input end ($z = 0$). Eventually, such saturation occurs at the 3 m region where the inversion is highest. This significantly depletes the entire inversion inside the amplifier. After this event, there will be little energy left for further pulse amplification. This inversion plot is consistent with the output power evolution as shown in figure 3.11.

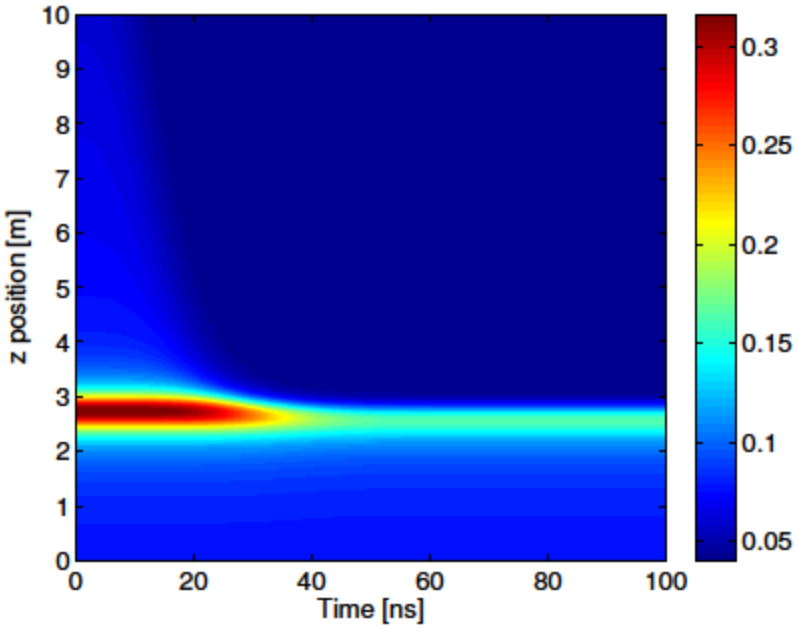

Figure 2.12 Dynamic change of the population inversion as a function of time and space.

On the other hand, the backward ASE reduces significantly once the inversion is drained by the forward pulse amplification. Figure 3.13 shows the backward ASE power as a function of time. Such reduction of backward ASE is clearly observed in the figure.

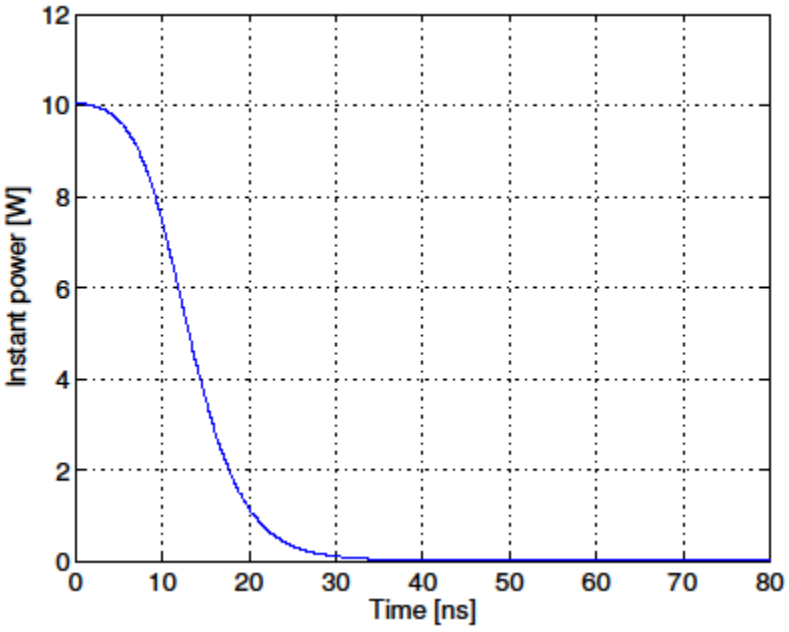

Figure 2.13 Backward ASE power time trace

Upwind and downwind combo method

We implemented the upwind and downwind combo method. Firstly, we checked the steady-state solution through the transient dynamics solver. The result is shown in figure 3.14. It is noted that the inversion is perfectly kept, unlike the Euler method or the Lax modification. As we have discussed, the reason is rather clear: there is no ambiguous calculation, which requires fictitious boundary values. The only drawback was the finer grid sizes for this method. We have used 800 grids along the z direction and the time gap was five times finer than the Courant condition. In the previous simulation of reduction method, we used only 200 grids in z direction and the time step was very large (one time Courant condition, which is actually 20 times larger than the upwind downwind combo method).

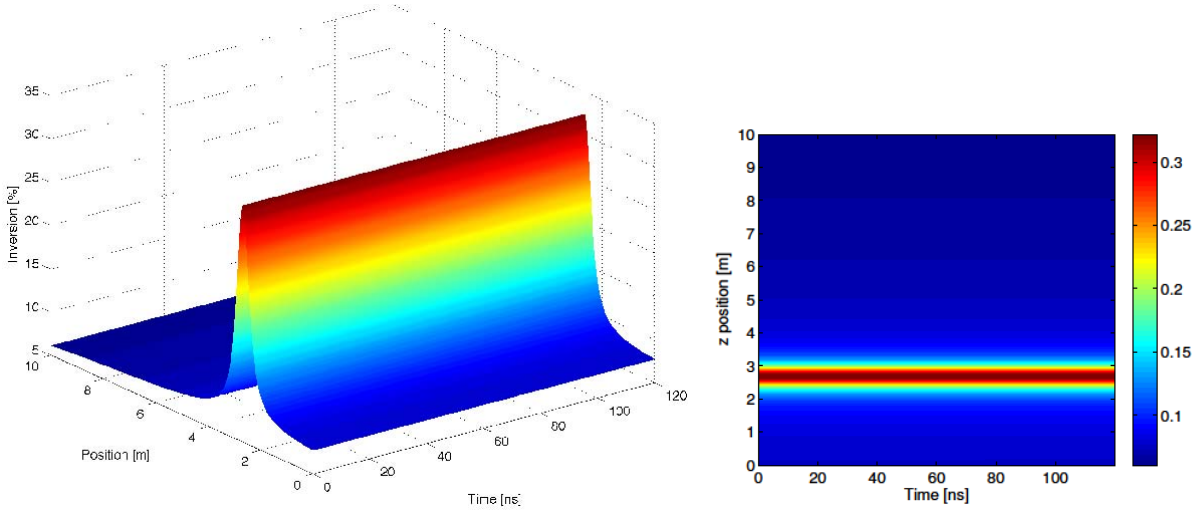

Figure 2.14 Obtained inversion as function of time and space, based on upwind downwind combo method.

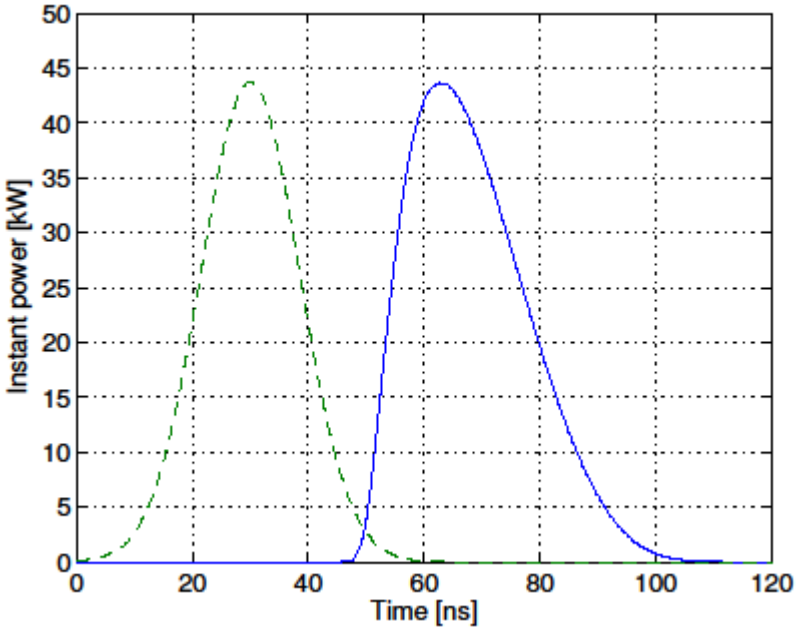

Figure 2.15 Output power time trace (blue) when 20 ns input pulse with 1 μJ at 1064 nm is injected (green). Please note that the input pulse is exaggerated by a factor of 930, in order to be compared easily with the output pulse.

We proceeded to the pulse amplification example. For this simulation, all the parameters are the same as the previous reduction method example. Figure 3.15 shows the output pulse time trace. It is remarkable that there is a time delay between the input pulse and the output pulse, which is approximately 50 ns as calculated from the speed of light inside the fiber and the fiber length. Please note that we have less time delay on the input and the output peaks, due to the early saturation phenomenon described in the previous section. The pulse shape, the duration, and the peak power are very similar to figure 3.11 except for the overall delay. Both results are also very similar to the result in reference [25]. This assures that both the reduction method and the upwind downwind combo method produced reasonable results in this case. Thus, the statement that the time delay can be ignored in many cases is quantitatively proven through these examples.

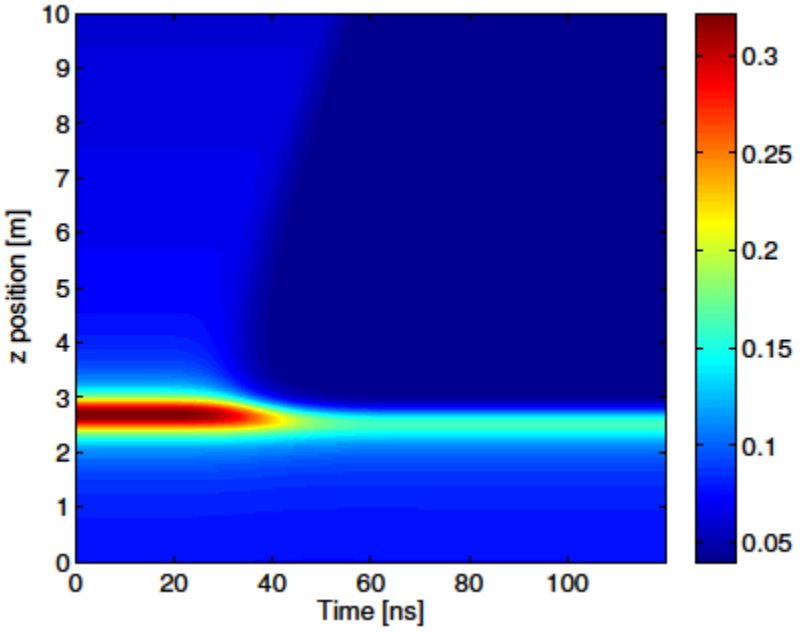

Figure 2.16 Dynamic change of the population inversion as a function of time and space.

Figure 3.16 shows the inversion dynamics as a function of both time and space. A remarkable difference from the previous example shown in figure 3.12 is the time delay of inversion depletion. The direction of depletion is now opposite compared to the previous simulation. This makes more physical sense since it will take propagation time to saturate the far end. Since the propagation time is 50 ns, we observe the inversion depletion at the output end after 50 ns of simulation time. The inversion dynamics is laterally shifted by 50 ns at the output end. Then, one might question how the output energy and pulse duration was very similar between the reduction method and the full partial differential equation solver. The reason is that the depletion time of the main inversion peak located at 2.8 m is very similar in both cases. The depletion patterns in the both cases are nearly identical. It is because the inversion before depletion was locally tightly concentrated. In this case, there is a very small difference between the reduction method and the full partial differential equation solver.
It is noteworthy that for reliable simulation the required grid size was more than 400 in the z direction and the time gap should be less than five times smaller than the Courant condition (25 ps). The simulation time in upwind downwind combo PDE solver was only 25 seconds.

3.2.3.3 Summary of numerical simulator development

We have developed a numerical simulator which solves (1) the transverse modes, (2) the steady-state solution, and (3) the transient solution and amplifier dynamics. Several different finite difference methods were tried. The simple and primitive finite difference method did not produce a stable numerical solution. Instead, it generated catastrophic numerical divergence, which started from numerical noise. The Lax modification was also tried. Unfortunately, however, the method did not work. It altered the steady-state condition by a diffusing process where locally

concentrated population inversion was gradually dissipated throughout the entire space. Lastly, the reduction method is implemented, which showed a very stable performance. The steady-state solution is perfectly preserved in the transient solver, which is a clear indication that the method effectively overcame the numerical noise. When compared with the published result, the method generated a very similar output pulse. The inversion dynamics, the forward output power, and the backward ASE transient behavior were all explained in a consistent manner.

The only approximation in the reduction method was to ignore the time derivative term in the power propagation differential equation, which can be justified when the pulse propagation time is shorter than other parameters. For the PG amplifier where the amplifier fiber length is about 10 cm, the propagation time is about 0.5 ns, which may be safely ignored for the input pulse duration of several nanometers. It is also noteworthy that the effect of propagation is in many cases ignorable so that many published modeling/simulation do not even include the time derivative in the power propagation from the beginning [10], [28], [29], [30], [31].

We also developed a full partial differential equation solver using the upwind and downwind combo method where the forward signal and pump is solved on upwind scheme whereas the backward signal and pump is solved on downwind scheme. This method eliminated any ambiguity on the boundary condition. Therefore, the steady-state was completely preserved in the transient solution, when there was no change in input power or pump powers. The developed simulator was extremely efficient, producing reliable results within a minute, thanks to the utilization of parallel computing and a multicore CPU. The pulse amplification example produces almost exactly the same result as the published paper.

The developed pulsed fiber amplifier simulator is different from previously published results and tools in that

1. The developed simulator solves pointwise inversion in 3D gain medium whereas the previously published results are based on averaged approach over the transverse plane. Therefore, this new tool enables a study on multimode fiber and the modal behavior in an accurate manner.
2. The simulator solves the transversal modes accurately. Especially when the fiber is bent, the simulator accurately calculates the bending loss for each guided modes.
3. With pointwise solving method, we can implement the thermal model or nonlinear optics model much more efficiently than the bulk approach.
4. Even with pointwise calculation, the simulation time is remarkably short. Most of the practical simulations in multimode fiber amplifier can be calculated within a minute.
5. The produced result is temporally, spectrally, modally, and spatially resolved. The output variables are thus 6-dimensional, which completely describes the light behavior. This produces a significant advantage, such as the access to the output beam quality.

4. FEASIBILITY STUDY FOR A HIGH ENERGY 2 MICRON FIBER LASER WITH LOW PHASE DISTORTION

4.1 Introduction

4.1.1 Motivation

A high energy pulsed source in the 2 μm wavelength region with narrowband spectral content would enable a range of remote sensing and communications applications. One potential application is remote sensing using optical heterodyne detection. The measurement requires the laser to be close to single-frequency (narrow optical bandwidth).

4.1.2 Goal to achieve

The laser requirement is summarized as follows.

Parameter	Value
Wavelength	2.05 μm
Seed power	1 mW (peak)
Seed spectral bandwidth	10 MHz
Repetition rate	1 - 10 kHz
Pulse duration	100 - 200 ns
Average output power	1 W
Output beam quality	Diffraction limited
Output spectral bandwidth	≤ 100 MHz

Table 4.1 Target laser specification

4.1.3 Obstacles to overcome

The laser requirement is challenging for several reasons. First, the output laser peak power must reach 10 kW, which in turn implies a net gain of 70 dB, starting from a 1 mW seed source. Such large overall gain cannot be achieved without multiple amplifier chains with careful junction control between the adjacent amplifiers. This includes removal of unwanted background amplified spontaneous emission (ASE), which spectrally and temporally adds unwanted background noise. Second, the narrow output spectral bandwidth can only be achieved through careful consideration of nonlinearity reduction strategy.

4.1.4 Problem solving strategy

We tentatively assume a simple laser system: seed laser, fiber amplifier chain with suitable level of gain for each amplifier, active time gating and passive spectral gating to remove the ASE, and

a specialty fiber amplifier for the final power amplifier, which dramatically reduces the nonlinearity, compared to the conventional FS fiber amplifiers. The questions we need to answer are

- How much gain can the first amplifier provide, without significant degradation from ASE?
- How much gain can the second amplifier provide, without significant degradation from ASE?
- With what power level a significant nonlinear degradation will happen? (Answer to this will lead to determine the input power to the final specialty power fiber amplifier.)
- What is the pulse energy we can obtain from the given design of the final specialty power fiber amplifier? This allowed energy will not suffer significantly from either stimulated Brillouin scattering or phase distortion (self-phase modulation).

In order to answer those questions, it is critical to develop a model and a simulator for the conventional and the specialty fiber amplifier, working at 2.05 μm. Once the model is established, a numerical simulator to obtain the output pulse parameters as a function of input pulse parameters and amplifier configuration will be developed. With the numerical simulator, the questions above will be answered one by one.

4.2 Modeling Tm-doped fiber amplifier

In this chapter, we will model a Tm-doped fiber amplifier. We first need to understand the spectroscopic characteristic of Tm-doped fiber.

4.2.1 Energy transition

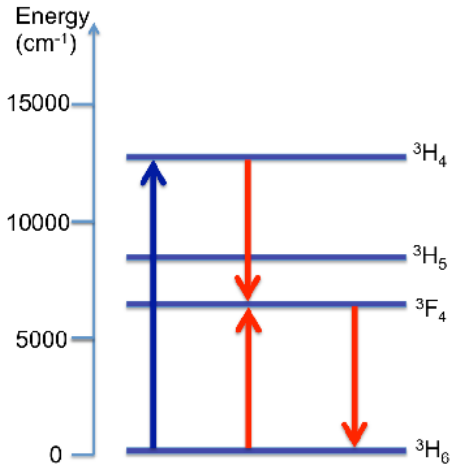

Figure 4.1 Schematic diagram of Tm^{3+}-ion energy transition.

Figure 4.1 shows the energy diagram of Tm^{3+}-ion and the energy transitions. A photon of 795 nm wavelength can pump the ion and excite to the energy level $^3H_4$. Once excited, the ion can quickly lose energy and stay on a lower energy level $^3F_4$. The lost energy sometimes can pump another ion in the ground state $^3H_6$ and excite it to the same energy level $^3F_4$. This process is particular to the Tm^{3+}-ion energy transition and it is called 'cross relaxation pumping' [32]. Although it is not shown in the figure, an undesirable effect also happens where the excited ion in $^3H_4$ falls to the energy level $^3H_5$ and then acquires the pump photon at 795 nm to jump up to a higher energy level $^1G_4$. In this case, the pump photon is (most likely) simply lost. This phenomenon is called 'energy transfer upconversion', which may or may not contribute towards the laser power [32]. The probability for such 'energy transfer upconversion' depends on the number of ions in the energy level $^3H_5$ and it again depends on the branching ratio of energy losing mechanism of ions in energy level $^3H_4$.
It must be noted that it is also possible to directly pump from the ground state to $^3F_4$ level, which is often called 'in-band pumping' as in Er-doped fiber amplifier pumped at 1480 nm. Even in this case, there is an upconversion process, where the excited ion at $^3F_4$ may absorb the pump photon and jump up to the energy level $^3H_4$. Depending on how the ion at $^3H_4$ loses its energy, it may or may not contribute towards the laser power.
Due to various loss mechanisms for the pumping photons, the thulium is not one of the most efficient doping ions from a laser efficiency point of view.

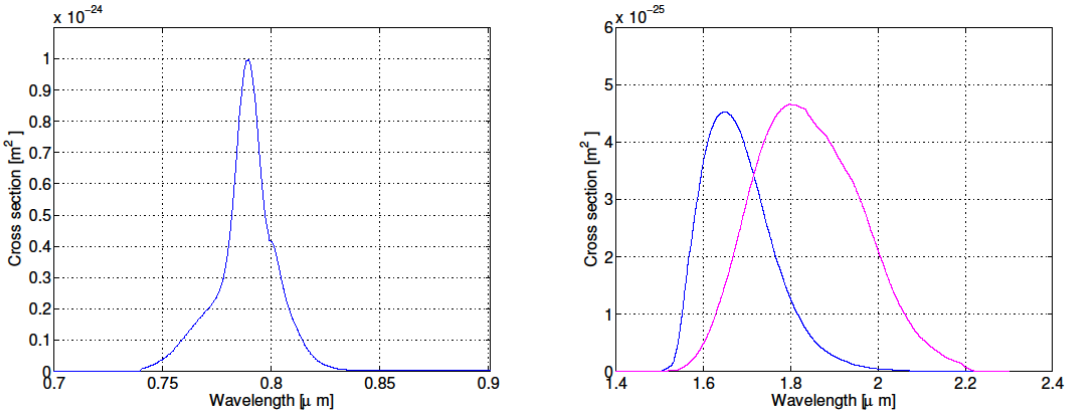

Figure 4.2 Absorption (blue) and emission (magenta) cross section of Tm^{3+}-ion in silica host.

4.2.2 Absorption and emission cross sections and excited ion lifetime

There are a number of published papers regarding the absorption and the emission cross sections of the Tm-doped fibers [33, 34]. Nufern independently performed the spectroscopic study on their own Tm-doped fiber samples. Their finding is that the result in [33] is closest to their own measurement. In addition, Nufern managed to convert the emission cross-section spectrum in the same reference to the absorption cross-section spectrum, using the McCumber relationship [35]. The decision of the zero-phonon energy in the McCumber relation is quite challenging. Nufern appeared to be resolved with multiple method combined, including direct measurement of the absorption spectrum.

Here, we take the emission and absorption cross section spectra from the two references [33, 36]. Figure 4.2 shows the absorption and emission cross section spectra of Tm^{3+}-ion. Please note that the data is taken from a Tm-doped FS fiber. The actual cross section spectrum may change depending on the host material. Apparently, there are two transitions shown in the spectrum: $^3H_6 \rightarrow {}^3H_4$ for 795 nm transition and $^3F_4 \rightarrow {}^3H_6$ for near 2 μm transition.
Tm^{3+}-ions have absorption and emission cross-section also in other wavelength regions, most notably at 1 μm region where there is a significant radiative transition between $^3H_6$ and $^3H_5$ energy levels. The absorption and the emission cross-section at this 1 μm region is nearly comparable to those at 2 μm region, which is however omitted in this report. We will consider a pumping wavelength exclusively at 0.8 μm wavelength. In this case, the energy level $^3H_5$ does not play a significant role.

4.2.3 Lifetime of excited Tm^{3+}-ions

There are three known energy relaxation mechanisms of an excited Tm^{3+}-ion. Firstly, the excited ion may emit a photon spontaneously and relax to lower energy levels. Secondly, it may interact with the glass network, which has quantized vibration modes. The excited ion may lose energy through multiple involvements of such glass vibration modes - phonons. The exchanged energy eventually is converted into heat. Finally, especially Tm^{3+}-ions may trigger the cross-relaxation process where the excited ion on $^3H_4$ energy level may exchange energy with ground-state ion and excite it to $^3F_4$ and relaxes to the same energy level itself. The result is that one pump photon may create two excited ions on $^3F_4$ energy level. Such cross-relaxation mechanism includes direct interaction and indirect interaction through phonons and photons. It is, however, apparent that higher Tm^{3+}-ion concentration will encourage the cross-relaxation process. Thus, the transition rate for the cross-relaxation will be naturally dependent on the Tm^{3+}-ion concentration.

4.2.3.1 Radiative decay

The radiative lifetimes are closely related to the wavelength-integral of the emission (absorption) cross-section. Judd-Ofelt analysis, in an assumption of negligible disturbances on 4*f* shell electrons, produces pure radiative lifetime (where the transition happens only through radiative decay). The published calculated pure radiative lifetimes are shown in table 4.2 [33]. Please note that the calculated pure radiative lifetimes are significantly different from measured lifetime, which is significantly affected by the other two mechanisms, particularly in Tm^{3+}-doped fibers.

Transition	Judd-Ofelt [33] [μs]	Measured [33] [μs]	Measured [37] [μs]
$^3H_4 \rightarrow {}^3H_6$	697	20	21
$^3H_5 \rightarrow {}^3H_6$	3896		
$^3F_4 \rightarrow {}^3H_6$	4559	420	540

Table 4.2 Lifetimes of Tm^{3+}-ions for various transitions. Comparison among Judd-Ofelt analysis and other published values.

4.2.3.2 Multiphonon relaxation

According to Layne et. al, the excited ion may relax through the energy exchange between the excited ions and the glass network vibration - phonons [38]. The host glass structure may have certain vibration patterns, which has specific frequencies. Due to the broad phonon spectrum, the excited ion may lose energy, relaxing to the next lowest level, by giving the excess energy to the phonon vibration modes. In case the energy gap is larger than the peak phonon energy frequency, multiple phonons may cooperatively absorb the energy from the excited ion. The multiphonon relaxation rate can be represented by [38]

$$W_{NR} \equiv C[n(T)+1]^{p} \exp(-\alpha \Delta E), \tag{4.1}$$

where C is a host dependent constant, $n(T)$ is the Bose-Einstein occupation number, given by

$$n(T) \equiv \frac{1}{exp\ (\hbar\omega/kT) - 1}, \tag{4.2}$$

where T is the temperature, $\hbar$ is the Planck constant ($\hbar = h/2\pi$), k is the Boltzmann constant, and ω is the phonon vibration frequency, which depends on the host material. In equation (4.1), α is also host dependent constant, ΔE is the energy gap between the excited level and the next lowest level, and p is the number of phonon involved, which is given as

$$p \approx \frac{\Delta E}{\hbar\omega}, \tag{4.3}$$

Table 4.3 summarizes some of the published numbers of the host dependent parameters. Layne et. al also measured the multiphonon relaxation rate. From the reference [38], one can extract the parameters of silicate glass host: $C = 9.24 \times 10^{12}$, $\alpha = 5.2 \times 10^{-3}$, and $\hbar\omega$ = 1100 [cm-1]. It is clear that the parameters vary significantly among the published results. Part of the reason is because measuring exclusively multiphonon relaxation is hard, due to various associated mechanism to relax the excited ions: these include radiative decay and cross-relaxation. For accurate measurement, it is necessary to reduce the doping concentration as much as possible, which ensures the exclusion of significant cross-relaxation effect.

Host matrix	C [s^{-1}]	$\hbar\omega$ [cm^{-1}]	α [cm]
Phosphate	5.4×10^{12}	1200	4.7×10^{-3}
Silicate	1.4×10^{12}	1100	4.7×10^{-3}
Borate	2.9×10^{12}	1400	3.3×10^{-3}
Tellurite	6.3×10^{10}	700	4.7×10^{-3}
Germanate	3.4×10^{10}	900	4.9×10^{-3}

Table 4.3 Parameters for nonradiative relaxation in glasses, taken from reference [39]

For instructive purposes, we can roughly calculate the multiphonon decay rate, using assumed parameters C and α. When we assume $\hbar\omega$ = 1100 cm^{-1} in FS fiber, using the values of $C = 1.4 \times 10^{12}$ s^{-1} and $\alpha = 4.7 \times 10^{-3}$ cm^{-1}, the calculated multiphonon decay times are

702 μs, 31 ns, and 1.15 s, respectively for the transitions $^3H_4 \rightarrow {}^3H_5$, $^3H_5 \rightarrow {}^3F_4$, and $^3F_4 \rightarrow {}^3H_6$. One remark is that the transition $^3H_5 \rightarrow {}^3F_4$ will be predominantly multiphonon relaxation, due to the extremely high rate of multiphonon relaxation.

4.2.3.3 Cross-relaxation

We now consider the cross-relaxation transition, which involves three energy levels $^3H_4$, $^3F_4$, and $^3H_6$. Although the center energy value of each level does not yield exactly the energy conserving cross-relaxation, the stark-split and homogeneously broadened energy level covers nonzero energy width for each energy level, which completes the cross-relaxation transition. For this, we consider a simplified rate equation for the fluorescence decay of the energy level $^3H_4$ as in [40, 41]:

$$\frac{dn_3}{dt} = -\frac{n_3}{\tau_{r,3}} - \frac{n_3}{\tau_{nr,3}} - k_{30} n_3 n_0 + k_{11} n_1^2, \tag{4.4}$$

where n_3, n_1, n_0 represent the ions concentration on energy levels $^3H_4$, $^3F_4$, and $^3H_6$, respectively, τ_r, τ_{nr} represent the radiative and the nonradiative lifetime, respectively. The last two terms describe the cross-relaxation rate and ks are the relevant coefficients.
In the limit where $n_0 \simeq N_0$ where N_0 is the Tm^{3+}-ion doping concentration, the equation (4.4) reduces to

$$\frac{dn_3}{dt} \simeq -n_3 \left(\frac{1}{\tau_{r,30}} + \frac{1}{\tau_{nr,32}} + k_{30} N_0 \right). \tag{4.5}$$

Then, the measured lifetime of the excited state $^3H_4$ can be represented as

$$\frac{1}{\tau_{m,3}} \simeq \frac{1}{\tau_{r,30}} + \frac{1}{\tau_{nr,32}} + k_{30} N_0, \tag{4.6}$$

which produces the cross-relaxation coefficient

$$k_{30} \simeq \frac{1}{N_0} \left[\frac{1}{\tau_{m,3}} - \frac{1}{\tau_{r,30}} - \frac{1}{\tau_{nr,32}} \right]. \tag{4.7}$$

We can also obtain k_{11} in a similar manner, by exciting the ion only to energy level $^3F_4$. Then, the rate equation for n_1 simplifies to

$$\frac{dn_1}{dt} \simeq -n_1 \left(\frac{1}{\tau_{r,10}} + \frac{1}{\tau_{nr,10}} \right) - k_{11} n_1^2, \tag{4.8}$$

which has an analytical solution:

$$n_1(t) = \frac{C}{e^{t/\tau_1} - Ck_{11}\tau_1}, \tag{4.9}$$

where $1/\tau_1 \equiv 1/\tau_{rad} + 1/\tau_{nrad}$. The above equation clearly implies that the measured lifetime will depend on the initial condition $n_1(t = 0)$, which is a function of both the inversion level and the doping concentration. Therefore, the typical lifetime measurement for the energy level $^3F_4$ will depend on the doping concentration and the pump intensity. By adjusting the exciting pump intensity, one can resolve the unknown C as well as the parameter k_{11}.

Assuming the density of Tm^{3+}-doped fiber as the same as FS (2.201 g/cm^3), 1 wt % Tm_2O_3 doping concentration yields 6.87×10^{19} ions/cm^3 of Tm^{3+}-ion concentration. With obtained pure radiative lifetime of 697 μs, the multiphonon decay time of 702 μs, and the measured fluorescence lifetime of 20 μs (with 1.44 wt % Tm_2O_3 doping concentration [33]) at energy level $^3H_4$, we can estimate k_{30} using equation (4.7). The result is $k_{30} = 4.8 \times 10^{-22}$ m^3/s/wt %. In addition, we can use the empirical relationship reported in [41]: $k_{11} = 0.084k_{30}$, we obtain $k_{11} = 4.0 \times 10^{-23}$ m^3/s/wt %.

Finally, table 4.4 summarizes the parameters for various decays discussed in this section.

Transition	Parameter	Value	Nature of transition	Obtained method
$^3H_4 \rightarrow {}^3H_6$	$\tau_{rad,30}$	697 μs	Radiative	Judd-Ofelt
$^3H_5 \rightarrow {}^3H_6$	$\tau_{rad,20}$	3896 μs	Radiative	Judd-Ofelt
$^3F_4 \rightarrow {}^3H_6$	$\tau_{rad,10}$	4559 μs	Radiative	Judd-Ofelt
$^3H_4 \rightarrow {}^3H_5$	$\tau_{nrad,32}$	702 μs	Multiphonon	Layne et. al
$^3H_5 \rightarrow {}^3F_4$	$\tau_{nrad,21}$	31 ns	Multiphonon	Layne et. al
$^3F_4 \rightarrow {}^3H_6$	$\tau_{nrad,10}$	1.15 s	Multiphonon	Layne et. al
$^3H_4$, $^3H_6 \rightarrow 2\ {}^3F_4$	k_{30}	4.8×10^{-22} m^3/s/wt %	Cross-relaxation	Petrin et. al
$2\ {}^3F_4 \rightarrow {}^3H_4$, $^3H_6$	k_{11}	4.0×10^{-23} m^3/s/wt %	Cross-relaxation	Petrin et. al

Table 4.4 Decay time of Tm^{3+}-ions for various transitions.

4.2.4 Rate equation

There are multiple ways to pump the Tm^{3+}-doped fiber. One can use a ~790 nm light source to pump from $^3H_6$ to $^3H_4$. Or one can use a ~1210 nm light source to pump from $^3H_6$ to $^3H_5$. Otherwise, one can use a ~1630 nm source to pump directly from $^3H_6$ to $^3F_4$.

For the case of pumping using a ~790 nm source, the rate equation for the Tm^{3+}-ions can be modeled as follows:

$$\begin{aligned} \frac{dn_3}{dt} &= W_{03} - \frac{n_3}{\tau_3} - k_{30}n_3n_0 + k_{11}n_1^2, \\ \frac{dn_1}{dt} &= 2k_{30}n_3n_0 - 2k_{11}n_1^2 - \frac{n_1}{\tau_1} + W_{01}, \end{aligned} \tag{4.10}$$

$$\frac{dn_0}{dt} = -W_{03} + \frac{n_3}{\tau_3} + \frac{n_1}{\tau_1} - W_{01} - k_{30} n_3 n_0 + k_{11} n_1^2,$$

where W_{03} is the pumping rate from energy level 0 ($^3H_6$) to 3 ($^3H_4$) and W_{01} is the signal photon contribution to the energy transition. They are given as

$$W_{03} \equiv \int_{\lambda_p} (\sigma_a n_0 - \sigma_e n_3) I_p \frac{\lambda}{hc} d\lambda,$$
$$W_{01} \equiv \int_{\lambda_s} (\sigma_a n_0 - \sigma_e n_1) I_s \frac{\lambda}{hc} d\lambda, \quad (4.11)$$

where I_p, I_s represents the light intensity of the pump and the signal, respectively, with an integral relation $\int_S \int_\lambda I \, d\lambda dS = P$ where S is the cross-sectional area of the fiber and P is the entire power. In equation (4.10), τ_i is the collective lifetime given as

$$\frac{1}{\tau_i} = \frac{1}{\tau_{r,i0}} + \frac{1}{\tau_{nr,i(i-1)}}, \quad (4.12)$$

where we ignored the negligible radiative transitions (e.g. $^3H_4 \rightarrow {}^3H_5$). We also assumed $n_2 \simeq 0$ since the multiphonon decay $^3H_5 \rightarrow {}^3F_4$ is very efficient with decay time in tens of nanoseconds.
A simple sanity check for the equation (4.10) is to check if the sum of left hand side and that of the right hand side of all equations results in zero. That is

$$\frac{d(n_3 + n_1 + n_0)}{dt} = 0. \quad (4.13)$$

This states the conservation of ions.
For the case of pumping using a ~1630 nm, the rate equation involves only n_0 and n_1, without the cross-relaxation terms in equation (4.10). That is

$$\frac{dn_1}{dt} = -\frac{n_1}{\tau_1} + W_{01},$$
$$\frac{dn_0}{dt} = \frac{n_1}{\tau_1} - W_{01}, \quad (4.14)$$

where

$$W_{01} \equiv \int_\lambda (\sigma_a n_0 - \sigma_e n_1)(I_s + I_p) \frac{\lambda}{hc} d\lambda. \quad (4.15)$$

Please note that this case becomes a two-level laser system.

The case of pumping using a ~1210 nm light source is the same as the above case of ~1630 nm since the nonradiative multiphonon transition $^3H_5 \rightarrow {}^3F_4$ will be sufficiently fast so that $n_2 \simeq 0$.

4.2.5 Pump and signal propagation

We present only the final equations here. Greater detail can be found in [42]. Firstly, if the pump light propagates in the core, the propagation equation of the pump is

$$\frac{n}{c}\frac{\partial I_p^{\pm}}{\partial t} \pm \frac{I_p^{\pm}}{\partial z} = \alpha_p I_p^{\pm}, \tag{4.16}$$

where n is the refractive index of the material, c is the speed of light, t is the elapsed time, z is the propagation distance, and $I_p^{\pm}$ represents the direction of pump propagation in either $\pm z$ direction. α_p is the 'gain' of the pump, which is given by

$$\alpha_p = N_0(\sigma_e n_2 - \sigma_a n_0) - \alpha_{p0}, \tag{4.17}$$

where α_{p0} is the intrinsic propagation loss of the fiber. Please note that we described a pointwise pump propagation, using a pump intensity I_p, instead of the entire power P_p. It is to include the spatially varying excited ion distribution. In case of cladding pumping, we assume a uniform pump intensity over the entire cladding cross-section. Also, the pump 'gain' changes to

$$\alpha_p = \frac{N_0}{A_{cl}}\int_{A_{cl}} (\sigma_e n_2 - \sigma_a n_0)\, dS - \alpha_{p0}, \tag{4.18}$$

where A_{cl} is the cladding area. We simply averaged the gain over the cladding area.
In order to describe the signal propagation, we decompose the signal into a superposition of transversal modes:

$$I_s = \sum_{i=1}^{N} (C_i^+ + C_i^-) I_i, \tag{4.19}$$

where i represents ith transversal mode and $C_i^{\pm}$ is the modal power of the positive and the negative propagating signal in mode i. $\bar{I}_i$ is the modal spatial intensity distribution with normalization rule $\int_S \bar{I}_i\, dS = 1$. Then we can describe the propagation of the power coefficients $C_i^{\pm}$:

$$\frac{n}{c}\frac{\partial C_i^{\pm}}{\partial t} \pm \frac{\partial C_i^{\pm}}{\partial z} = \alpha_i C_i^{\pm} + C_0, \tag{4.20}$$

where the signal gain α_i is

$$\alpha_i \equiv N_0 \int_S (\sigma_e n_1 - \sigma_a n_0) I_i dS - \alpha_{i0}, \tag{4.21}$$

where α_{i0} is the intrinsic loss of ith mode. In equation (4.20), the spontaneous emission term C_0 is given by

$$C_0 \equiv \frac{2N_0 hc^2 \sigma_e}{\lambda^3} \left[\frac{1}{A_{co}} \int_S n_1 \, dS \right]. \tag{4.22}$$

Please note that we have fully integrated in our model the following:

- Spatially varying light intensity and the inversion distribution.
- Both forward and backward pump and signal.
- Spontaneous emission and the amplified spontaneous emission.
- Partial differential equation, describing not only the static change of power, but also the time-varying power dynamics.

The established model here is truly one of the most sophisticated and 'complete' laser dynamics models, except for the higher order nonlinearity, which will be introduced in the following section.

4.2.6 Fiber nonlinearities

With the listed target specification in table 4.1, we anticipate several nonlinear mechanisms that may potentially degrade the performance. These are self-phase modulation (SPM), stimulated Brillouin scattering (SBS), and stimulated Raman scattering (SRS). The SPM may disturb the optical phase within the pulse envelope and create new frequency components. Thus, it needs to be limited. The SBS may arise, due to the narrow bandwidth output at high power, which interact with the phonons through sound wave. The SBS will create new wavelength components (albeit close to the signal), propagating in the opposite direction. This new wave may extract the energy from the main pulse, which needs to be amplified. The SRS arises due to the interaction between the signal and the glass phonons, creating new wavelength component at Stokes wavelength. This Raman signal may extract energy from the main signal, preventing the amplification. Other than these, the self-stiffening and the intrapulse Raman scattering can hinder the performance.

4.2.6.1 Self-phase modulation, self-stiffness, and intrapulse Raman scattering

Nonlinear optical Kerr effect describes the change in refractive index as a function of optical power. This causes the SPM, self-stiffness, and the intrapulse Raman scattering [43]. These three nonlinearities can be modeled and can be integrated into the propagation equations in the previous section, which is, however, not desirable since it may make the equations numerically stiff. Instead, we obtain the gain profile of the amplifier along the propagation distance z and

model the self-phase modulation separately from the rate equation and power propagation equation. According to reference [43], the wave equation can be modeled as

$$\frac{\partial A}{\partial z} + \frac{g(z)}{2}A + \frac{i\beta_2}{2}\frac{\partial^2 A}{\partial T^2} - \frac{\beta_3}{6}\frac{\partial^3 A}{\partial T^3} = i\gamma\left(|A|^2 A + \frac{i}{\omega_0}\frac{\partial}{\partial T}(|A|^2 A) - T_R A\frac{\partial |A|^2}{\partial T}\right), \quad (4.23)$$

where A is the electrical field with $P_s = |A|^2$, $g(z)$ the gain profile along z, $\beta_2, 3$ the second and the third order dispersion coefficient, γ the nonlinear coefficient of the fiber, ω_0 the carrier angular frequency, and T_R the Raman coefficient. The nonlinearities listed on the right hand side alters the phase and, thus, optical spectrum eventually. The dispersion terms on the left hand side may change the temporal pulse shape. Here, T is different from $t$since $T = t - z/v_g$ where v_g is the pulse's group velocity.

Thus, we will first find out the gain profile $g(z)$ by solving the power propagation equations in the previous section. Then, we will incorporate the obtained $g(z)$ into the equation (4.23) to obtain the distortion on the temporal and spectral properties of the pulse. The equation (4.23) can be solved through the split-step Fourier method as in [43].

4.2.6.2 Stimulated Brillouin scattering

Stimulated Brillouin scattering describes light scattering as an interaction between the photons and the phonons (vibration modes) of the glass network. Such glass vibration can be caused by the photon-phonon interaction, which propagates to some distance. This vibrational propagation appears as a sound wave. It is rather obvious that light with a large coherence (a smaller optical bandwidth) will suffer more from the SBS. Light with a narrow spectrum will give rise to well-defined sound waves with a narrow band, which coherently add together to become very large number of phonons.

There are numerous SBS models published. A general review of many different models of SBS can be found in [44]. Still, the validity of the models is debated. For now, it is wise to stay with one of the most widely used simple models based on Smith's paper [45], which calculates the SBS threshold power to be

$$P_{SBS} \simeq \frac{21A_{eff}}{g_B L_{eff}}\left(1 + \frac{\Delta\omega_s}{\Delta\omega_B}\right), \quad (4.24)$$

where A_{eff} is the effective core area, $L_{eff} \equiv [1 - \exp(-\alpha_s L)]/\alpha_s$ is the effective length where α_s is the loss (or gain when negative), L is the fiber length, and $\Delta\omega_s$ is the signal optical bandwidth (FWHM), $\Delta\omega_B$ is the Brillouin gain bandwidth in FS fiber and is approximately $2\pi \times 30$ MHz. The Brillouin gain coefficient g_B is approximately 5×10^{-11} m/W in FS fiber, depending on wavelength, etc. More detail can be found either in [43] or [45]. Please note that this calculation has limitations since (1) it is based on a very long pulse approximation where the pulse duration is much longer than the sound-wave lifetime ($\sim$ 90 ns) and (2) it is for a mono-mode FS fiber.

In this model, we will check the approximate SBS threshold power for a given geometry of fiber and amplifier configurations since finding out the detailed dynamics of the Brillouin Stokes wave is not our primary concern.

5. CONCLUSIONS

Single-transverse-mode output energy of 0.7 mJ at 1.03 μm has been demonstrated using large core (35 um diameter) highly Yb-doped PG fibers, and 2.25 mJ has been demonstrated with multimode output using 49 μm core PG fibers. The attainable energy was limited by optical damage resulting from excessively high peak intensity. The duration of the input pulses available for these experiments limited our ability to reduce the peak power and increase output energy. Longer pulses (>10 ns) would likely allow higher energies to be attained with the existing fiber architecture. The energies achieved using the largest core fibers (49 μm) were consistent with a damage threshold of 250W/um^2. The 0.7 mJ single-mode output had a peak power of approximately 70 kW, and work performed elsewhere on PG fibers with smaller cores has demonstrated that single-frequency output can be achieved using higher intensities in comparably short fibers. Therefore we anticipate that single-frequency multi-mJ pulses can be attained using the methods demonstrated here if ~100 ns single-frequency input pulses are available. Single-mode amplification was demonstrated using tapered multimode fibers (35 um core) with modestly low NA of 0.05. Larger core fibers with this NA could not be tapered because of limitations to the tapering equipment. If fibers with lower NA can be obtained, single-mode propagation using larger cores may be attainable using the techniques demonstrated here, further extending performance. Therefore, substantial enhancement of the performance of single-frequency pulsed amplifiers should be available through modifications to the input pulse and fiber NA. Progress toward the development of a narrowband source for the 2 um region was also demonstrated, which provides a basis for further work in this area. A fiber amplifier model was developed that is capable of simulating the behavior of highly-doped fiber amplifiers as well as conventional fiber amplifiers.

6. REFERENCES

1. Campbell, J.H. and T.I. Suratwala, *Nd-doped phosphate glasses for high-energy/high-peak-power lasers.* Journal of Non-Crystalline Solids, 2000. **263**(1-4): p. 318-341.
2. Lee, Y.W., et al., *10-Watt, Single-mode, Single-frequency, 1.03 mu m Yb(3+)-doped Phosphate Fiber Amplifier.* 2008 Conference on Lasers and Electro-Optics & Quantum Electronics and Laser Science Conference, Vols 1-9, 2008: p. 230-231.
3. Petersen, E., et al., *High peak-power single-frequency pulses using multiple stage, large core phosphate fibers and preshaped pulses.* Applied Optics, 2012. **51**(5): p. 531-534.
4. Galvanauskas, A., et al., *High peak power pulse amplification in large-core Yb-doped fiber amplifiers.* Ieee Journal of Selected Topics in Quantum Electronics, 2007. **13**(3): p. 559-566.
5. J.P. Koplow, e.a., Sandia Report, SAND2009-0860, 2009.
6. Brooks, C.D. and F. Di Teodoro, *Multimegawatt peak-power, single-transverse-mode operation of a 100 mu m core diameter, Yb-doped rodlike photonic crystal fiber amplifier.* Applied Physics Letters, 2006. **89**(11).
7. Stacey, C.D., et al., *Demonstration of fundamental mode only propagation in highly multimode fibre for high power EDFAs.* Optics Communications, 2007. **269**(2): p. 310-314.
8. A. W. Snyder, J.D.L., *Optical Waveguide Theory.* Chapman and Hall, London, 1983.
9. Jackson, S.D., et al., *High-power 83 W holmium-doped silica fiber laser operating with high beam quality.* Optics Letters, 2007. **32**(3): p. 241-243.
10. Smith, A., *Private communication.* 2007.
11. Marcuse, D., *Theory of dielectric optical waveguides.* Academic Press, 1991.
12. Marcuse, D., *Curvature loss formula for optical fibers.* Journal of Optical Society of America, 1976. **66**(3): p. 216-220.
13. Marcuse, D., *Field deformation and loss by curvature of optical fibers.* Journal of Optical Society of America, 1976. **66**(4): p. 311-320.
14. Cole, R.T.S.a.J.H., *Improved bend loss formula verified for optical fibers by simulation and experiment.* IEEE Journal of Quantum Electronics, 2007. **43**(10): p. 899-909.
15. Agrawal, G.P., *Optical pulse propagation in doped fiber amplifiers.* Physical Review A, 1991. **44**: p. 7493-7501.
16. Desurvire, E., *Erbium-doped fiber amplifiers.* Wiley, 1994.
17. Hardy, A., *Signal amplification in strongly pumped fiber amplifiers.* IEEE Journal of Quantum Electronics, 1997. **33**(3): p. 307-313.
18. Agrawal, G.P., *Nonlinear fiber optics.* Academic Press, 2001. **3rd Ed.**
19. W.J. Miniscalo, R.S.Q., *General procedure for the analysis of er^{3+} cross sections.* Optics Letters, 1991. **16**(4): p. 258-260.
20. W.B. Fowler, D.L.D., *Relation between absorption and emission probabilities in luminescent centers in ionic solids.* Physical Review, 1962. **128**(5): p. 2154.
21. M. Gong, Y.Y., C. Li, P. Yan, H. Zhang, and S. Liao, *Numerical modeling of transverse mode competition in strongly pumped multimode fibers lasers and amplifiers.* Optics Express, 2007. **15**(6): p. 3236-3246.
22. M. Devautour, P.R., and S. Fevrier, *3D modeling of modal competition in fiber laser: Application to HOM suppression in multi-layered fiber.* Conference on Lasers and Electro-Optics, 2009.

23. W.H. Press, S.A.T., W.T. Vetterling, and B.P. Flannery, *Numerical recipes.* Cambridge University Press, 3rd ed., 2007.
24. Thomas, J.W., *Numerical partial differential equations - finite differences methods.* New York: Springer-Verlag, 1995.
25. Y. Wang, H.P., *Dynamic characteristics of double-clad fiber amplifiers for high-power pulse amplification.* Journal of Lightwave Technology, 2003. **21**(10): p. 2262-2270.
26. R. Paschotta, J.N., A.C. Tropper, and D.C. Hanna, *Ytterbium-doped fiber amplifiers.* IEEE Journal of Quantum Electronics, 1997. **33**: p. 1049-1056.
27. J.R. Marciante, J.D.Z., *High-gain, polarization-preserving, Yb-doped fiber amplifier for low-duty cycle pulse amplification.* Applied Optics, 2006. **45**(26): p. 6798-6804.
28. Y. Sintov, O.K., Y. Glick, S. Acco, Y. Nafcha, A. Englander, and R. Lavi, *Extractable energy from ytterbium-doped high-energy pulsed fiber amplifiers and lasers.* Journal of Optical Society of America B, 2006. **23**(2): p. 218-230.
29. Y. Sun, G.L., J.L. Zyskind, A.A.M. Saleh, A.K. Srivastava, J.W. Sulhoff, *Model for gain dynamics in erbium-doped fiber amplifiers.* Electronics Letters, 1996. **32**(16): p. 1490-1491.
30. Y. Sun, J.L.Z., A.K. Srivastava, *Average inversion level, modeling, and physics of erbium-doped fiber amplifiers.* IEEE Journal of Selected Topics in Quantum Electronics, 1997. **3**(4): p. 991-1007.
31. A. Bononi, L.A.R., *Doped-fiber amplifier dynamics: a system perspective.* Journal of Lightwave Technology, 1998. **16**(5): p. 945-956.
32. Jackson, S.D., *Cross relaxation and energy transfer upconversion processes relevant to the functioning of 2 mu m Tm3+-doped silica fibre lasers.* Optics Communications, 2004. **230**(1-3): p. 197-203.
33. Walsh, B.M. and N.P. Barnes, *Comparison of Tm : ZBLAN and Tm : silica fiber lasers; Spectroscopy and tunable pulsed laser operation around 1.9 mu m.* Applied Physics B-Lasers and Optics, 2004. **78**(3-4): p. 325-333.
34. Agger, S.D. and J.H. Povlsen, *Emission and absorption cross section of thulium doped silica fibers.* Optics Express, 2006. **14**(1): p. 50-57.
35. Mccumber, D.E., *Einstein Relations Connecting Broadband Emission + Absorption Spectra.* Physical Review a-General Physics, 1964. **136**(4A): p. A954-&.
36. Nufern, *Cross section measurement of thulium doped fibers.* Private correspondence, 2010.
37. Moulton, P.F., et al., *Tm-Doped Fiber Lasers: Fundamentals and Power Scaling.* Ieee Journal of Selected Topics in Quantum Electronics, 2009. **15**(1): p. 85-92.
38. Layne, C.B., W.H. Lowdermilk, and M.J. Weber, *Multiphonon Relaxation of Rare-Earth Ions in Oxide Glasses.* Physical Review B, 1977. **16**(1): p. 10-20.
39. Reisfeld, R. and M. Eyal, *Possible Ways of Relaxations for Excited-States of Rare-Earth Ions in Amorphous Media.* Journal De Physique, 1985. **46**(C-7): p. 349-355.
40. R.R. Petrin, M.G.J., R.C. Powell, M. Kokta, *Spectral dynamics of laser-pumped $Y_3Al_5O_{12}$: Tm, Ho lasers.* Optical Materials, 1992. **1**(2): p. 111-124.
41. Jackson, S.D. and T.A. King, *Theoretical modeling of Tm-doped silica fiber lasers.* Journal of Lightwave Technology, 1999. **17**(5): p. 948-956.
42. Soh, D.B., *Development of all-fiber passively q-switched laser: Modeling and simulation.* Technical Report SAND2011-4269, Sandia National Laboratories, 2011. **June**.

43. Agrawal, G., *Nonlinear fiber optics.* Nonlinear Science at the Dawn of the 21st Century, 2000: p. 195-211.
44. A. Kobyakov, M.S., D. Chowdhury, *Stimulated brillouin scattering in optical fibers.* Advances in Optics and Photonics, 2010. **2**(1): p. 1-59.
45. Smith, R.G., *Optical Power Handling Capacity of Low Loss Optical Fibers as Determined by Stimulated Raman and Brillouin-Scattering.* Applied Optics, 1972. **11**(11): p. 2489-2494.

DISTRIBUTION

1	MS1218	Briggs Atherton	05944
1	MS9056	Wen Hsu	08128
1	MS9056	Ray Bambha	08128
1	MS9056	Mark Dansson	08128
1	MS9056	Sean Moore	08128
1	MS9056	Daniel Soh	08128
1	MS0899	Technical Library	9536 (electronic copy)
1	MS0359	D. Chavez, LDRD Office	1911


Sandia National Laboratories